TECHNISCHE
UNIVERSITÄT
WIEN
Vienna University of Technology

Comparison of peri-implant loading in screw-bone constructs predicted by homogenized and micro FE models

DIPLOMA THESIS

carried out for the purpose of obtaining the degree of Master of Science (Dipl.-Ing. or DI)
submitted at TU Wien Faculty of Mechanical and Industrial Engineering
Institute of Lightweight Design and Structural Biomechanics

by

Lukas Ortner
[redacted]

under supervision of:

Univ.Prof. Dipl.-Ing. Dr.techn. Dieter Pahr
Co-supervisor Dipl.-Ing. Dr.techn. Alexander Synek, MSc

Vienna, 11th May, 2022

Affidavit

Affidavit
I declare in lieu of oath, that I wrote this thesis and performed the associated research myself, using only literature cited in this volume. If text passages from sources are used literally, they are marked as such.
I confirm that this work is original and has not been submitted elsewhere for any examination, nor is it currently under consideration for a thesis elsewhere.
I acknowledge that the submitted work will be checked electronically-technically using suitable and state-of-the-art means (plagiarism detection software). On the one hand, this ensures that the submitted work was prepared according to the high-quality standards within the applicable rules to ensure good scientific practice "Code of Conduct" at the TU Wien. On the other hand, a comparison with other student theses avoids violations of my personal copyright

Vienna, 11th May, 2022

Acknowledgements

I would like to thank my supervisor Dr. Dieter Pahr, who always gave me constructive feedback, which I greatly appreciated.

I would also like to say a big thank you to Dr. Alexander Synek, who gave valuable feedback and guided me through this work .

I would also like to thank my family and friends who have supported me throughout my education.

Kurzfassung

Eine wichtige Art der Frakturbehandlung ist die interne Fixierung komplizierter Knochenfrakturen durch Platten und Schrauben oder durch Knochenschrauben. Eine besonders häufige Fraktur ist die distale Radiusfraktur. Bei instabilen Frakturen hat sich die interne Stabilisierung mit einer volaren Verriegelungsplatte zu einer Standardmethode entwickelt. Eine unzureichende Verankerung der Schraube im Knochen kann jedoch zu einer Lockerung führen. Simulationen von Schrauben-Knochen-Konstrukten ermöglichen es, Forschungsfragen mit relativ geringen Kosten und ohne die Notwendigkeit wertvoller Gewebeproben, wie sie in Experimenten notwendig sind, zu untersuchen. Besonders Simulationen mit Finite-Elemente (FE)-Modellen haben dabei an Popularität gewonnen. Zwei häufig verwendete Arten von FE-Modellen sind Mikro-Finite-Elemente-Modelle (μFE) und homogenisierte Finite-Elemente-Modelle (hFE). μFE-Modelle sind genau und relativ einfach zu erstellen, erfordern jedoch mehr Rechenleistung. hFE-Modelle hingegen bieten einen recheneffizienten Modellierungsansatz. Die Mikroarchitektur des trabekulären Knochens wird jedoch nicht berücksichtigt (mm Elementgröße) und Materialeigenschaften werden basierend auf homogenisierten Materialeigenschaften abgeschätzt. Diese Studie untersucht die Beziehung der periimplantären volumengemittelten Verzerrungsenergiedichte (SED) zwischen hFE und μFE von Einzelschrauben-Knochen Konstrukten. Der Vergleich sollte mit verschiedenen hFE-Modellierungsstrategien unter verschiedenen Lastfällen erfolgen. Neun μCT-Scans von distalen Radiusabschnitten dienten als Grundlage dieser Studie. Aus den Radiusabschnitten wurde eine zylindrische Knochenprobe virtuell entnommen und eine Schraube virtuell implantiert. Für jede Knochenprobe wurden zwei unterschiedliche Belastungsfälle (axialer Auszug und Scherung) analysiert. Nach dem Lösen der FE-Modelle

wurden benutzerdefinierte Skripte verwendet, um die Ausgabe auszuwerten. Die Ausgabe umfasste: 1) Steifigkeit, 2) Verzerrungsenergiedichten, gemittelt in einem zylindrischen Volumen um die Schraube. Die Ausgabe wurde für jede der neun Knochenproben, beide Lastfälle und beide Modelltypen (hFE, μFE) ausgewertet. In einem klinischen Szenario (inklusive eines Kortex) eines einzelnen Schrauben-Knochen-Konstrukts am distalen Radius wurde eine signifikante Korrelation zwischen den durchschnittlichen Verzerrungsenergiedichten (SED) des periimplantären Volumens und zwischen der Federsteifigkeit von hFE und μFE-Modelle in zwei Lastfällen gefunden. hFE-Modelle überschätzten die Steifigkeit und unterschätzten die volumengemittelten Verzerrungsenergiedichten. Der Unterschied zwischen hFE und μFE zeigte eine Abhängigkeit von knochenmorphometrischen Parametern und war besonders hoch bei Proben mit geringem Knochenvolumenanteil. Eine Teilstudie zur Modellierungsstrategie des trabekulären Knochenmaterials in den hFE-Modellen zeigte, dass die lokale Orthotropie des trabekulären Knochens die Genauigkeit und Präzision der Vorhersage der SED-Verteilung nur geringfügig verbesserte. Insgesamt zeigte diese Studie, dass hFE-Modelle volumengemittelte periimplantäre SEDs von Schraubknochenkonstrukten in guter Übereinstimmung mit μFE-Ergebnissen vorhersagen können, aber diese Übereinstimmung kann sich bei Knochenproben mit geringer Knochenvolumenqualität drastisch verschlechtern.

Abstract

An important mode of fracture treatment is the internal fixation of complicated bone fractures with plates and screws or with bone screws. A particularly common fracture is the distal radius fracture. For unstable fractures, internal stabilization with a volar locking plate has become a standard method. However, insufficient anchoring of the screw in the bone can lead to loosening. Simulations of screw-bone constructs allow research questions to be addressed at relatively low cost and without the need for valuable tissue samples such as are necessary in experiments. In particular, simulations with finite element (FE) models have gained popularity. Two commonly used types of FE models are micro finite element models (μFE) and homogenized finite element models (hFE). μFE models are accurate and relatively easy to create, but require more computational power. hFE models, on the other hand, offer a computationally efficient modeling approach. However, trabecular bone microarchitecture is not considered (mm element size) and material properties are estimated based on homogenized material properties. This study investigates the relation of peri-implant volume-average strain energy density (SED) between hFE and μFE of single-screw bone constructs. The comparison should be made with different hFE modelling strategies under different load cases. Nine μCT scans of distal sections of the radius served as the basis of this study. A cylindrical bone sample was taken virtually from the radius sections and a screw was virtually implanted. Two different load cases (axial pull-out and shear) were analyzed for each bone sample. After solving the FE models, custom scripts were used to evaluate the output. The output included: 1) stiffness, 2) strain energy densities averaged in a cylindrical volume around the screw. The output was evaluated for each of the nine bone samples, both load cases and both model types (hFE, μFE).

In a clinical scenario (i.e., including both trabecular bone and cortex) of a single screw-bone construct at the distal radius, a significant correlation was found between the mean strain energy densities (SED) of the peri-implant volume and between that of the spring stiffness of hFE and μFE models in two load cases. hFE models overestimated stiffness and underestimated volume-average strain energy densities. The difference between hFE and μFE showed a dependence on bone morphometric parameters and was particularly high in samples with low bone volume fraction. A sub-study on the modeling strategy of the trabecular bone material in the hFE models showed that the local orthotropy of the trabecular bone improved the accuracy and precision of the prediction of the SED distribution only slightly. Overall, this study showed that hFE models can predict volume-averaged peri-implant SEDs of screw bone constructs in good agreement with μFE results, but this agreement can degrade dramatically in bone samples with low bone volume quality.

Contents

CHAPTER 1

Introduction

1.1 Motivation

Many fractures require surgical treatment with osteosynthetic devices [1]. Osteosynthesis is the fixation of a bone fracture with an implantable device. An important mode of fracture treatment is the internal fixation of complicated bone fractures by plate and screw or by bone screws alone [2, 3]. A particularly frequent fracture is the distal radius fracture, which is a fracture in close proximity to the joint [4]. In case of unstable fractures, internal fixation with a volar locking plate has become a standard method. In volar locking plates, the screws have self-cutting screw heads which engage with the implant plate and form an angular-stable construct to keep the fracture fragments in place [5].
However, insufficient support of the screw in the bone might lead to loosening. As a result, the reduction could be lost (malunion) or the fracture might not heal at all (nonunion) [6]. In severe cases, revision surgery might be necessary [7]. A study by Kralinger et al. [8] showed that 35% of 150 patients after fixed-angle plate fixation had mechanical failure, loss of reduction and secondary screw loosening.

To investigate the risks and effects of mechanical failure, typically experimental in vitro testing of the implant-bone constructs using cadaveric bones is performed [5, 9, 10]. However this approach is time consuming and requires human specimens

[11] or synthetic bone which cannot fully capture the material properties of real bone [12]. Computer simulations of screw-bone constructs allow investigating research questions with relatively low cost and without the need of valuable tissue samples as necessary in experiments. Especially simulations with finite element (FE) models have gained popularity in this process [13]. Two frequently used types of FE models are micro finite element (μFE) models and homogenized finite element (hFE) models.

μFE models are accurate and relatively easy to create, but they demand more computational resources [14]. This is especially seen in non-linear analyses. hFE models on the other hand provide a computationally efficient modeling approach [15], even in case of nonlinearity [14]. However, the microarchitecture of trabecular bone is not directly considered in hFE models (mm element size) [16]. Instead, the material properties are derived based on homogenized material properties, which rely on the local bone morphometry (e.g. bone density). Furthermore, the overall modelling process, including material mapping and meshing, can be more challenging compared to µFE models.

In the following chapters, the background and state of the art of screw-bone construct biomechanics and FE modelling are explained (section 1.2 to 1.5), followed by the specific goals of this thesis (section 1.6).

1.2 Mechanics of Bone and Bone-Screw Interface

1.2.1 Bone

Bone material consists of carbonated hydroxyapatite (HA), collagen protein (mostly collagen type I), many other non-collagenous proteins and water [17]. Bone has a hierarchical structure that differs across the length scales [18]. These hierarchical structures are shown in Figure 1.1 from left to right: the macrostructure, which consists of cortical and cancellous bone (porous bone composed of trabeculated bone tissue); the microstructure, consisting of osteons and single trabeculae; the sub-microstructure consisting of lamellae; the nanostructure consisting of fibrillar collagen and lastly the sub-nanostructure that houses molecular structure of constituent elements (e.g. mineral and collagen) [19]. This hierarchical structure gives bone anisotropic and heterogenous properties.

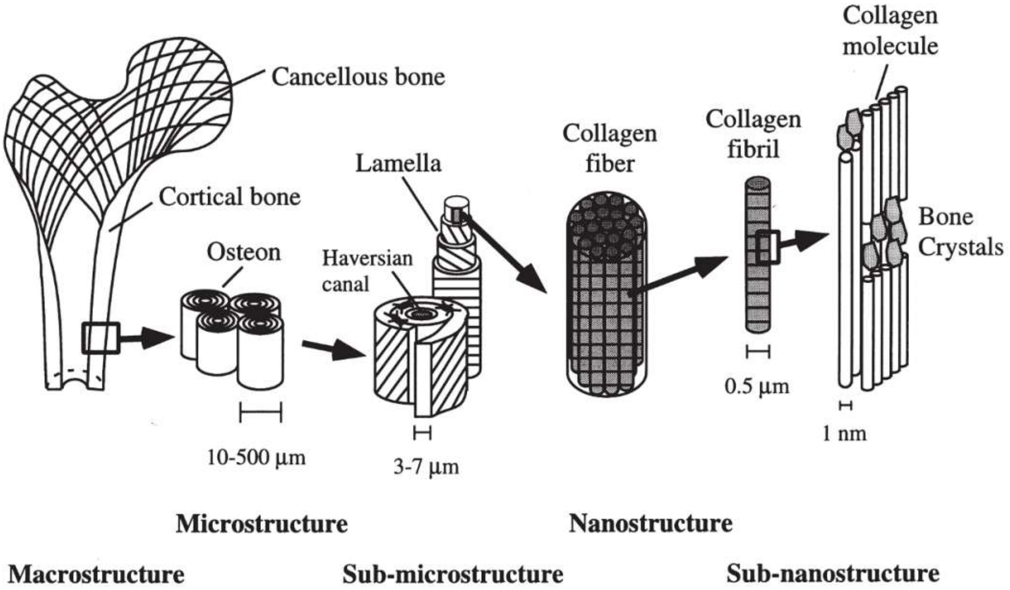

Figure 1.1: Hierarchical structure of bone from macrostructure to sub-nanostructure. Reproduced with permission from Rho et al. [19]

At the macrostructure bone is divided into cortical and trabecular bone. The differentiation is mostly given by the degree of porosity or density. Trabecular bone has a porosity of 40% to 95% and cortical bone has a porosity of 5% to 15% [20]. Long bones typically have a dense cortical shell that encapsulates a porous trabecular bone. Trabecular bone is made of trabecular struts (also called trabeculae) and marrow-filled cavities [21]. The trabeculae are interconnected and enclose the cavities [22]. In general, the mechanical properties of bones vary at the macrostructural level depending on the bone type and within regions of the same bone [19].

Strength and tensile/compressive moduli of cortical bone are smaller along radial/circumferential directions and greater along the longitudinal direction [20]. If the bone is loaded in tension along the longitudinal direction, it exhibits a linear stress-strain relation in the elastic region (see Figure 1.2 a). After the elastic region, a yield point is reached followed by strain hardening that ends at a fracture strain of less than 3%. In compressive loading, when the yield point is reached, a rapid hardening occurs, followed by softening and fracture at roughly 1.5% strain. The ultimate strength of bone (maximum load it can carry before breaking) depends on the mode of loading. The material bone is stronger in compression than tension and weaker in shear [20].

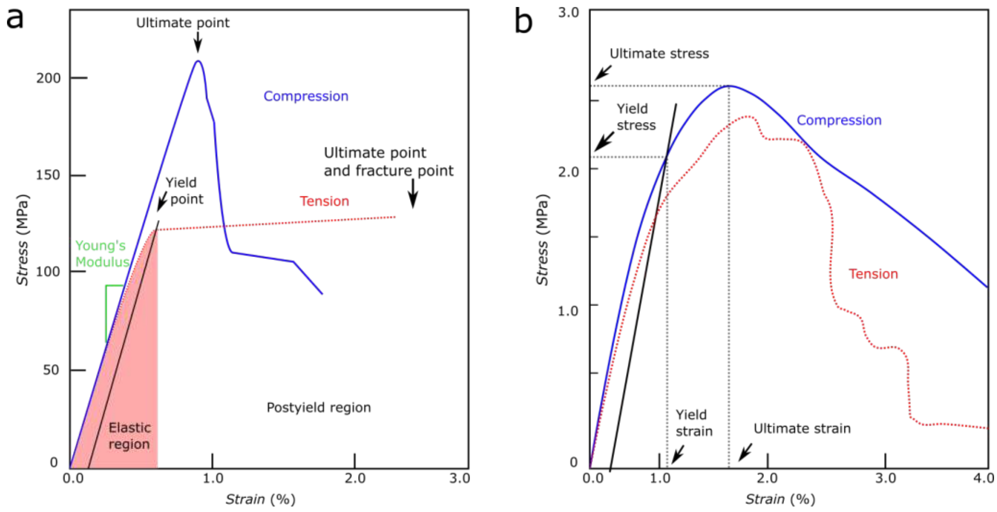

Figure 1.2: Stress strain curves for monotonic tests in tension and compression of cortical bone (a) tested along the longitudinal direction and trabecular bone (b) tested along the principal direction (based on [20]).

For trabecular bone the mechanical properties are mostly determined by the porosity [20]. Secondary parameters include the arrangement of the trabecular network and the tissue properties of individual trabeculae. Similar to cortical bone, trabecular bone strength is greater in compression than tension and lowest in shear. In compressive loading trabecular bone yields at strains of 0.7%, however, it can sustain strains up to 2.2% while still maintaining a large portion of the load-bearing capacity (see Figure 1.2 b) [20].

1.2.2 Screw-bone Interface

Bone screws are widely used devices for fixation or stabilisation [23]. Bone screws work through the conversion of torque into internal tension in the screw and the elastic reactions in the bone surrounding the screw [24]. This creates compression between the screw and the fracture fragments, which hold the screw together. The determining factors of the screw mechanics are the outer and base diameter and the thread pitch and angle. A prerequisite for the success of the entire fixation construct is safe anchoring [25]. As the screw is pulled out of trabecular bone, it cuts or shears bone as the screw-threads move outward and trap the bone in the threads [26]. The stability of bone-screw constructs mainly depends on the interface between bone and screw thread [1, 3]. Damage occurs during screw insertion and the interface is not fixed immediately after screw implantation. With locking screws in combination with a plate acting as a load-bearing device, the screw head locks to the plate, enabled by a locking mechanism through a self-tapping thread that cuts into the plate, forming a rigid plate-screw construct (e.g. volar locking plates) [27].

1.3 Finite Element Method

1.3.1 Basic Concepts for Biomechanical Applications

Since the 1970's the finite element method (FEM) has been used in biomechanical problems and has been proved as a powerful tool [28]. The breakthrough of FEM becoming the basis of *in silico* trials can be attributed to the rise of computational power. Complex biomechanical problems that are difficult to solve *in vivo* or *in vitro* may be investigated by FEM in ways that otherwise would not be possible. These biomechanical problems can be solved by FEM, which is a numerical technique that approximates the solutions to partial differential equations [29]. FE analyses in biomechanics consist of three important parts: the mesh representing the geometry of the tissue, material properties of the elements and the boundary conditions applied to the mesh [14]. Computational models used for FEM are usually created by using data from magnetic resonance imaging (MRI) and X-ray (micro-) computed tomography (μCT,CT) scanners [28]. The images acquired by diagnostic imaging tools are further processed to obtain 3D surface models in a relevant digital format, which are then processed to obtain a finite element mesh. Two frequently used types of FE models are micro finite element (μFE) models and homogenized finite element (hFE) models.

μFE models are generated from high-resolution μCT images (resolution of around 30μm). The images are then converted into hexahedron elements which capture the microarchitectural variation in trabecular bone [7]. μFE models are accurate and relatively easy to create, but extremely computationally intensive and time-consuming. Substantial computational resources are needed to simulate an entire bone/implant system, particularly if non-linearities (e.g. material, geometry) should be included [30, 31].

In a typical hFE model, the microarchitecture of trabecular bone is not considered in the mesh (mm element size), but material properties of each element are derived based on homogenized material properties which rely on local bone morphometry (e.g. local bone density). However, hFE models still provide a computationally efficient modeling approach to simulate whole bones with implants [15]. They are easily extendable to non-linear behaviour [14] and can be run on standard PCS, compared to μFE models [30]. Furthermore, the overall modelling process, including material mapping and meshing, can be more challenging compared to µFE models. [14].

1.3.2 Homogenization of Bone Tissue

Many materials bear heterogenous structures and their physical properties depend on their underlying microstructure, which may differ in various instances, such as volume fraction [32]. The fundamental goal of the homogenization method is the estimation of effective macroscopic properties of a heterogenous material with it's underlying microstructure, and to map this information on an equivalent substituted homogeneous material. There are two general methods in modelling heterogenous materials [33]: The unit cell method, based on detailed modeling

of the microstructure, leading to a macroscopic constitutive model and the direct micro-macro method as a generalization to the first method. These methods are based on the concept of a representative volume element (RVE) [33, 34]. A RVE represents a point of a continuum field that approximates the true micro-structured material. The RVE is defined in two situations: a unit cell in a periodic structure and a volume containing a very large portion of microscale elements (Figure 1.3). In the case of a RVE, the boundary conditions are defined such that the Hill-Mandel condition holds, preserving the equivalence of elastic energy between the scales, meaning the average of microscopic strain energy density (SED) is the same as the macroscopic SED. The Hill-Mandel condition further states, as long as the surface values of traction and displacement are macroscopically uniform the apparent moduli are independent of the surface values of displacement and traction [32, 33]. In that sense "effective" properties rather than "apparent" properties are obtained. However, in the case of trabecular bone the same theory can't be applied which means the boundary conditions (BCs) will always influence the predicted elastic properties. Therefore, instead of a RVE for trabecular bone the term volume element (VE) was introduced. Transitioning between the micro- and macroscale is realized through averaging the internal fields within the RVE.
A study by Pahr et al. [33] compared uniform displacement BCs (KUBCs), uniform traction BCs (SUBCs), periodicity compatible mixed uniform BCs (PMUBCs) and periodic BCs (PBCs) human trabecular bone. Among others, it was stated that in the case of porous micro structures, displacement based BCs are required to obtain average strains directly from the resulting strains. It could be seen that PMUBCs and PBCs gave the same effective elastic material behaviour and KUBCs hugely overestimated elastic material parameters, especially for bone with lower density. To be a statistical representative of the composite the RVE must be large enough to include all heterogeneities of the microstructure but at the same time the RVE needs to be adequately small to be considered a volume element in terms of continuum mechanics [32].

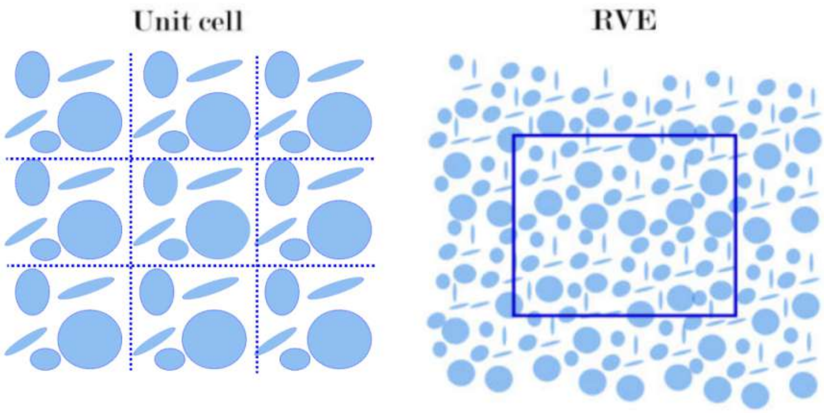

Figure 1.3: Situations for a RVE: unit cell in a periodic structure and a volume containing a very large portion of microscale elements (based on [33, 34])

1.3.3 Material Mapping

As explained in Section 1.3.2 computational homogenization is a method to model hierarchical materials. The parameters of the microstructure are used to compute equivalent strength and stiffness at the macrostructure. This section explains how the inhomogeneous material parameters at the macroscale can be mapped to individual elements of the FE mesh of a hFE model.

For modeling bone there are two factors to consider: trabecular bone has different properties than the cortical layer and the material property distribution is not homogeneous [35]. After the FE mesh has been generated, material properties have to be assigned to each element [36]. Bone density is shown to be related to mechanical properties of bone tissues. Therefore, the mechanical properties (e.g. density, fabric) should be derived directly from CT data. Meshes can be categorized into voxel-meshed (hexahedral mesh) and smooth-meshed (tetrahedral mesh) geometries [30]. Material mapping of voxel-based meshes is simple and can be highly automated by mapping gray values from the CT images to elasticity constants. Alternatively for smooth-meshed geometries material mapping algorithms that map local bone density into an elastic modulus can be used. Examples for such mapping algorithms include the algorithm of Pahr et al. [14], which uses a regular background to evaluate bone morphometry in several volume elements and then

linearly interpolates the material properties for all elements. Material models for these smooth models with material mapping include power laws, that map the local bone density into an elastic modulus for isotropic density based materials but also Zysset Curnier [37] orthotropic fabric-elasticity relationship.
The influence of material mapping was shown in different studies: A study by Synek et al.[38] showed that the implementation of local bone density improved the stiffness prediction compared to homogeneous bone models of fractured distal radii with volar locking plate treatment. In another study by Pahr et al. [33] vertebral bodies with a density and fabric based cancellous bone material and KUBCs provided statistically equivalent structural predictions as μFE models.

1.3.4 Modelling the Screw-Bone Interface

Stability of bone-screw constructs mainly depend on the interface of bone and screw threads [1, 3]. There are several ways to model screw-bone interfaces in FE that have been explored in studies (e.g. sliding with friction) [1]. However, the most common approach is to assume a fully bonded interface ("osseointegrated") [39, 40]. This approximation simplifies the analysis by making it linear [1]. However, it must be mentioned that in reality, damage will occur during screw insertion and the interface will not be tied directly after screw implantation. Ovesy et al. [31] and Macleod et al. [1] reported that the local stresses and strains within the bone near the screw had a significant dependence on the interface modelling. Thus, studies assuming fully bonded interfaces may be valid to predict "secondary stability", but not primary stability (directly after screw insertion) [7, 41].

1.4 State of the Art

In this thesis, hFE and μFE models of screw-bone constructs should be investigated. Numerous previous studies have used either μFE or hFE to simulate bone-screw constructs [42, 43, 44], but direct comparisons are scarce.
Wirth et al. [39] compared heterogeneous and homogeneous μFE models using trabecular bone samples of varying density and virtually implanted screws of different lengths. The bone-screw interface was assumed as fully bonded. They

demonstrated that the peri-implant strains cannot be determined accurately using the homogeneous model. However, in that study, homogeneous material properties were assigned to the entire bone as a simplification and the cortex was not modeled. The introduction of heterogeneity of bone has been shown to significantly affect the stiffness prediction of hFE models of fractured distal radii with volar locking plate treatment [38].

Chevalier et al. [40] compared μFE and hFE models using trabecular bone samples of the proximal humerii and virtually implanted a corkscrew anchor. The bone-implant interface was assumed as fully bonded. This study included heterogeneity of bone through material mapping without trabecular orientation, but excluded the cortex. They showed that despite differences in the stress distributions, the structural stiffness of the hFE models created from the same images with isotropic behaviour have shown excellent correlation with a μFE approach. These correlations suggest that simplified hFE models can be used to perform structural investigations.
Varga et al. [11] showed that average elastic strain around the screw, predicted using hFE models, correlates well with construct failure of locked plated proximal humerus fractures. The assumption was that the failure is dominated by trabecular bone with a constant yield strain and failure was defined by the number of load cycles until a critical plastic deformation was reached. Linear hFE models were used to evaluate peri-implant bone strains. Despite the simplification of the screw shafts to be modeled as idealized cylinders without threads, the results show that the peri-implant strain field by hFE modelling is an efficient predictor of construct failure. It's worth mentioning that this research included the cortex representing a clinical scenario (i.e., including both trabecular bone and cortex) as compared to research of Wirth et al. [39] and Chevalier et al. [40] and the screw shafts were tied to trabecular bone. However, this comparison was done with an experimental model and not directly with a μFE model as opposed to Wirth et al. [39] and Chevalier et al. [40].
In contrast to screw-bone constructs, more studies have compared μFE and hFE models of intact bone and generally found a good agreement between the two

methods [45, 46, 47]. For instance, Hosseini et al. [45] showed that the hFE approach is a promising time-efficient diagnostic tool for identifying patient-specific bone stiffness and failure load.

1.5 Gap

Previous studies have shown that the distribution of μFE and hFE peri-implant loading does not coincide locally [39]. However, an experimental study by Varga et al. [11] showed that peri-implant load averages are good predictors of implant failure. The question arises, why peri-implant load averages are good predictors of failure despite possible inaccuracies. There are several explanations.
The previous studies so far did not consider the cortex in the model, which deviates from the typical clinical scenario where screws are anchored unicortically and in the trabecular bone. Furthermore, different material modeling strategies were found in the studies. Wirth et al. [39] used homogeneous material properties and only one load case, while Chevalier et al. [11] used inhomogeneous material without anisotropic material behaviour.

1.6 Thesis Goals

In conclusion, research comparing hFE and μFE models of screw-bone constructs is limited and so far led to conflicting results. There is evidence that local peri-implant stress or strain peaks cannot be captured using hFE models. However, previous research suggests structural parameters (e.g. stiffness) or volume-averaged peri-implant loading (e.g. strains) are clinically valuable parameters that might be predicted with sufficient accuracy using hFE.
This study investigates the relation of hFE and μFE peri-implant strain energy densities (SED) volume averages of single screw bone constructs. The comparison should be done in nine specimens with different hFE modelling strategies under different load cases including both trabecular bone and cortex.

The specific research questions of this study thus are as following:

1. Do the hFE and μFE peri-implant strain energy densities (SED) volume averages correlate in bone samples including both trabecular and cortical bone?
2. Does the local correlation of peri-implant SED of hFE models improve by using orthotropic and inhomogeneous trabecular bone material properties instead of isotropic homogeneous or isotropic inhomogeneous properties?

CHAPTER 2

Material and Methods

2.1 Methodological Outline

The methodological approach was separated in three steps: (1) image preprocessing, (2) finite element analysis and (3) data processing and evaluation (2.1).

Graphical summary of the methodology (Figure 2.1) in brief , nine μCT scans of the distal radius sections were obtained from a previous study [48]. The images were already resampled to 32.8 μm resolution from the previous study and segmented into bone and background voxels. A cylindrical bone sample was extracted from the radius sections and a screw was virtually implanted. The screw geometry was obtained from a μCT scan of a screw of a volar locking plate system, resampled to 32.8μm resolution.
The images were preprocessed in the script manager Medtool (v4.5, Dr. Pahr Ingenieurs e.U., Pfaffstätten, Austria). Medtool is a work-flow management system that provides a 3D image processing platform and is able to generate simulation models from 3D medical images. The main image processing steps included transformation for uniform sample alignment, masking to extract a cylindrical region and boolean operations to insert the screw. After the image preprocessing, bone morphometrics were evaluated (e.g. bone density, cortical thickness) and used to calculate material properties for bone in the homogenized FE analysis (FEA).

hFE models were created in the script manager Medtool and solved with Abaqus (Dassault Systèmes Simulia Corporation, Rhode Island, USA[49]) and μFE models were created in Medtool and solved with ParOSol (ParOSol, Cyril Flaig[50]). Two different load cases (axial pullout and shear) were analyzed for each bone sample.

After solving the FE models, custom scripts written in the Python programming language (Python Software Foundation[51]), were used to evaluate the output. The output included: 1) structural stiffness in two directions, 2) strain energy densities, averaged in a cylindrical volume of interest (VOI) around the screw. The output was evaluated for each of the nine bone samples, both load cases and both model types (hFE, μFE). Each of the three main steps (image preprocessing, finite element analysis, data processing and evaluation) will be explained in the following sections in more detail.

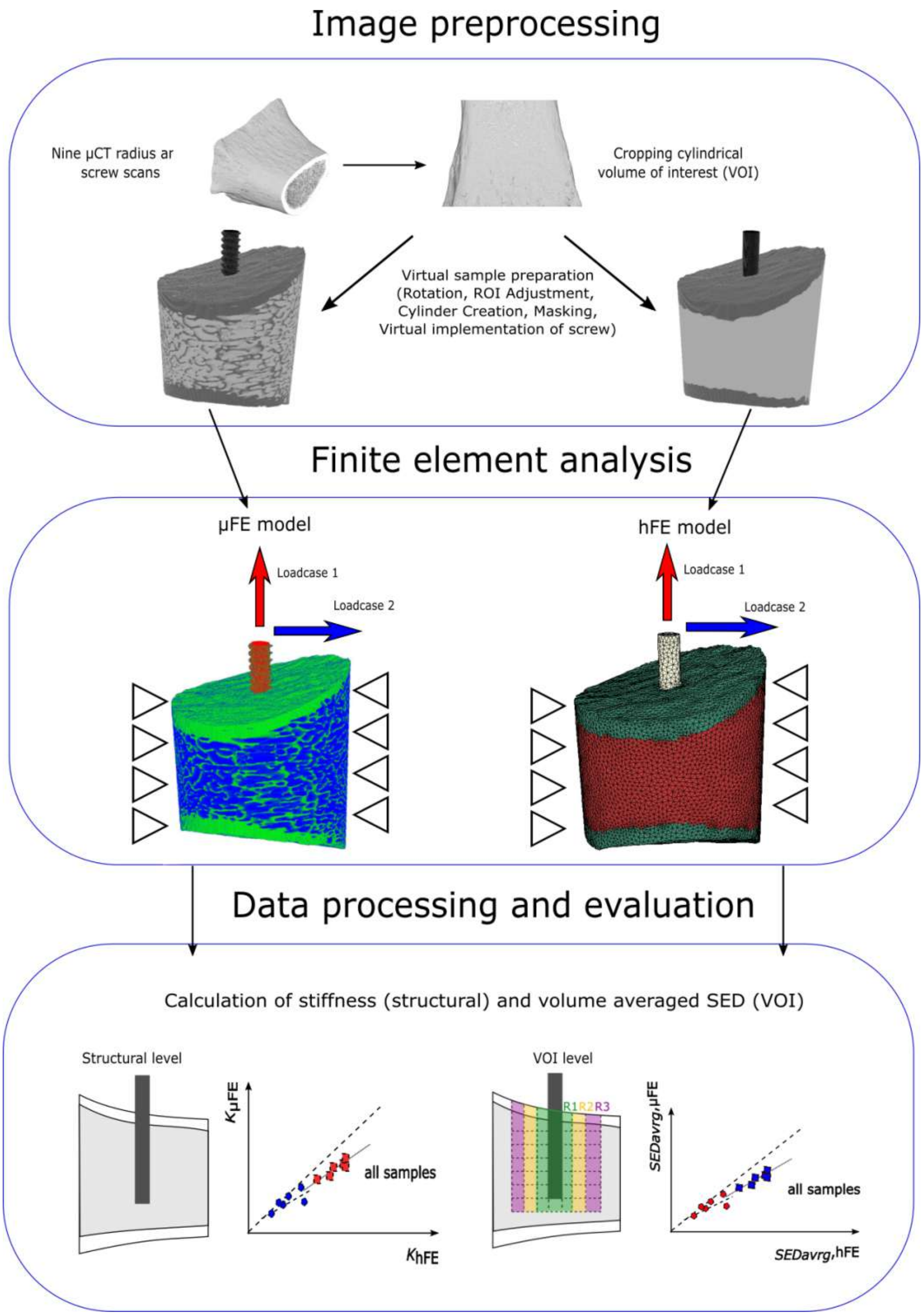

Figure 2.1: Outline of the methods used in this study. First, μCT images were processed to obtain bone samples with virtually inserted screw (1), then, μFE and hFE models were generated and analyzed (2), and finally, predicted stiffness and volume average SEDs were compared between μFE and hFE models (3).

2.2 Image Preprocessing

This section describes how screw and bone images from Stipsitz et al. [48] were processed and combined in order to create cylindrical bone samples with virtually implanted screws. Based on these images, hFE and μFE models should be created as described in section 2.3. In addition, the evaluation of bone morphometry is described. This section is divided into

1. Radius scans
2. Virtual sample preparation
3. Evaluation of bone morphometrics

2.2.1 Radius Scans

Sample ID	Year of birth	Gender	Side
179	1943	male	left
182	1933	female	right
186	1945	male	right
189	1933	male	left
193	1943	male	left
195	1943	female	left
196	1934	female	right
200	1926	male	right
203	1934	male	left

Table 2.1: Specimen overview

Nine μCT scans of the distal radius sections of the left and right radii were obtained from a previous study [48] (see Table 2.1 and Figure 2.2 a). The images were already resampled to 32.8 μm resolution from the previous study and segmented into bone and background voxels (see Figure 2.2 b). In addition, cortical and trabecular bone masks were available for each sample (see Figure 2.2 c).

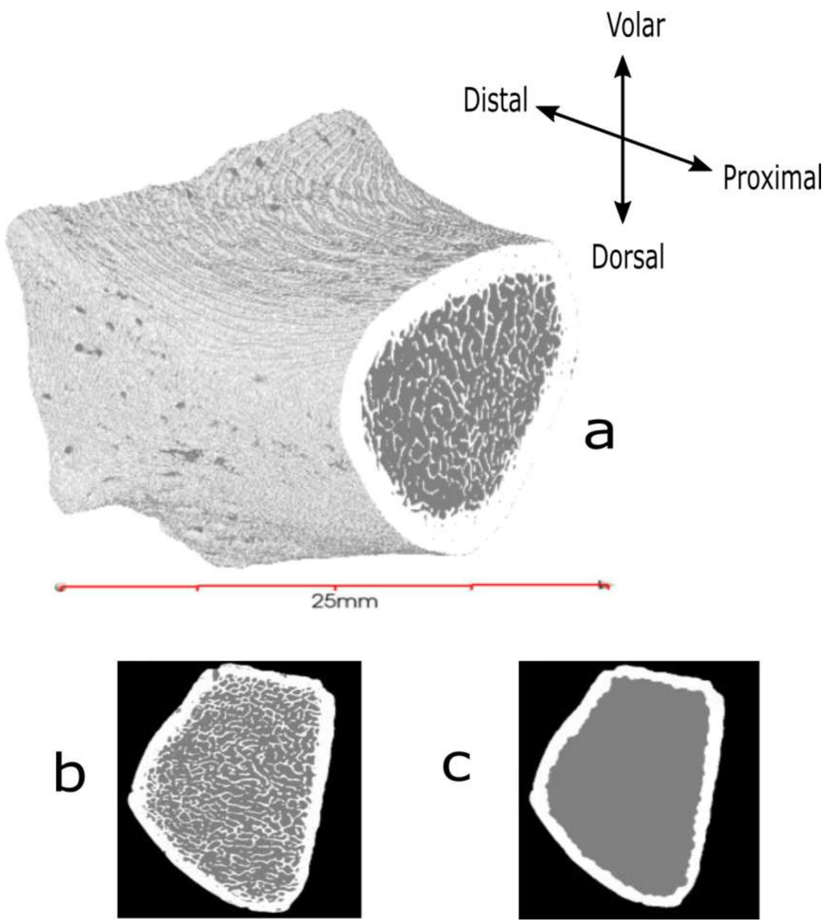

Figure 2.2: a) μCT scan of a distal radius sample; b) Transversal cross section of the distal radius and c) its corresponding trabecular bone mask

2.2.2 Virtual Sample Preparation

For virtual sample preparation, the geometry of a screw was needed. For this purpose, a μCT scan of a Medartis locking screw (A-5750, Medartis Inc., Basel, Switzerland), resampled to 32.8μm resolution, was used. The screw had to be segmented and correctly aligned for further processing. Next, bone samples had to be aligned and a cylindrical VOI had to be cropped out. Finally, the screw and bone samples had to be combined. First, a histogram (see Figure 2.3) of the gray scale of the image was created to find a threshold for segmenting the screw and to remove the bone material which was also visible in the scan.
The chosen threshold from the histogram for segmenting the screw was 80. Note

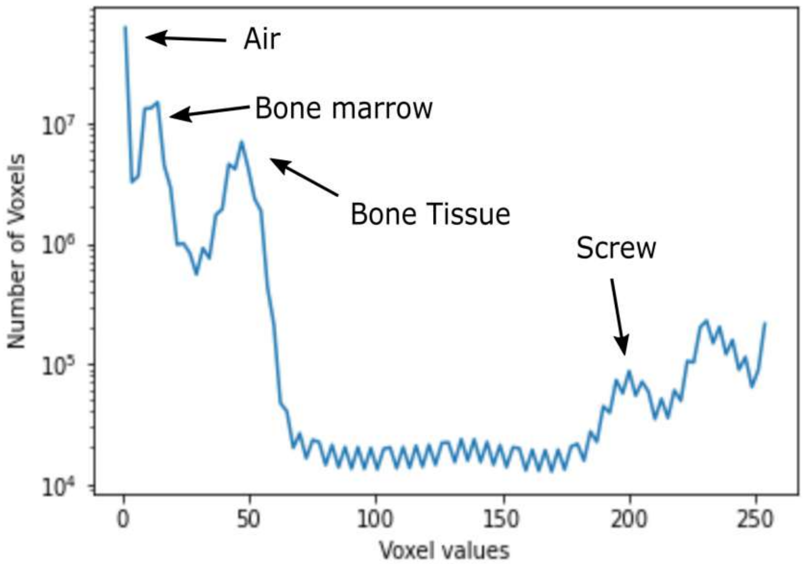

Figure 2.3: Distribution of the voxel gray values in the μCT image of the screw.

that the gray values of the screw showed two distinct peaks in the histogram because the middle part of the screw, which was inserted into cortical bone in the μCT scan (Figure 2.4a), had lower grey values than the rest of the screw. Gray values below 80 were assigned a gray value of zero and gray values above 80 were assigned a gray value of one. Additionally, a morphological closing and island removal algorithm was applied to remove unwanted noise from the image while preserving the shape and size of the screw and deleting unconnected areas of floating voxels.

Next, the axis of the screw had to be determined, to align the screw image. The screw image was loaded in 3D Slicer[52](https://www.slicer.org/) and the centroidal screw tip position and the centroid of the screw head were manually selected. This process was repeated multiple times and averaged to account for reproducibility and scatter effects. These two points were used for calculating the rotation matrix and represented the coordinates of the screw tip centroid and the screw head centroid. The calculation of the rotation matrix is shown in Algorithm 2.1.

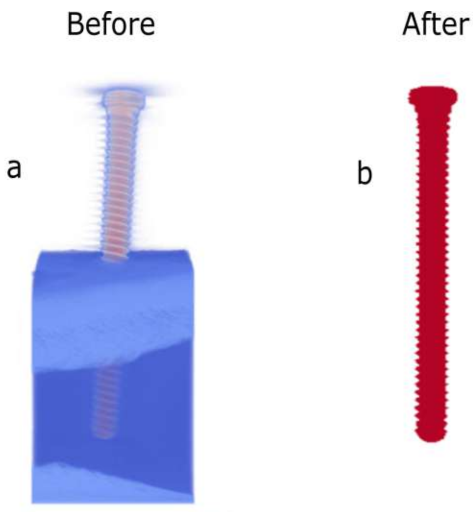

Figure 2.4: a) Screw before and b) after segmentation and rotation

Algorithm 2.1: Calculation of rotation matrix

Input: Screw tip and screw head centroid points

Output: Rotation matrix

1 Acquire screw axis vector: screw tip and screw head centroid points

2 Define and normalize the screw axis as a 3D vector

3 Normalize screw axis vector as basis vector $\underline{\mathbf{e}_x}$

4 Choose any normalized vector normal to $\underline{\mathbf{e}_x}$ as $\underline{\mathbf{e}_y}$ of the new basis

5 Cross product to get :

$$\underline{\mathbf{e}_z} = \underline{\mathbf{e}_x} \times \underline{\mathbf{e}_y} \tag{2.1}$$

6 Rotation matrix

$$\underline{\underline{\mathbf{R}}} = \begin{bmatrix} \underline{\mathbf{e}_x} & \underline{\mathbf{e}_y} & \underline{\mathbf{e}_z} \end{bmatrix}^T \tag{2.2}$$

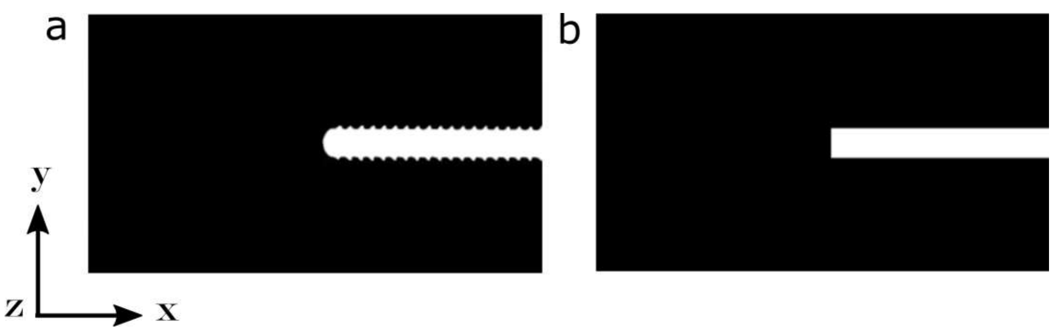

Figure 2.5: The final orientation of the a) screw and the b) cylinder

The rotation matrix obtained from Equation 2.2 was used for the rotation transformation filter in Medtool to obtain the correctly rotated screw (see Figure 2.4 b). The rotated screw image was cropped so that only the screw remained in the image. This was necessary in order to symmetrically expand the image to a specific size of 30.93mm times 17.74mm. The screw was shortened to a length of 15mm and rotated in a way that the longitudinal axis of the screw was aligned with the x-axis of the specimen (see Figure 2.5 a).
For the hFE models, an unthreaded cylinder was used instead of a screw. The cylinder was created as an image using Medtool and aligned consistently with the screw. The cylinder was also cropped and aligned the same way as the screw. The diameter of the cylinder was the volume-equivalent diameter of the screw (2mm) and both, cylinder and the screw, were each 15mm in length (see Figure 2.5).

Next, the images of the distal radii had to be rotated, to ensure consistent specimen alignment. All radius scans were rotated such that the screw could be virtually inserted from the volar side.
With the use of 3D Slicer, fiducial points were set along the surface line of the volar side of the radii in a centered transverse cross section (see Figure 2.6). The entire image was then rotated until the fiducial points were aligned vertically. The acquired rotation angles were then used to rotate each sample individually using the rotation transformation filter in Medtool.
The radius images had three gray values (zero = air, one = bone marrow and two = bone). To account for interpolation effects during rotation, the samples were segmented into two parts shown in Figure 2.7, where one was devoted to bone marrow and the other to bone only. After the segmentation of both parts, the images were rotated, interpolated and finally put together again into one image. This was done through the summation of the gray values of both segmented parts. The same rotation method was applied to the trabecular and cortical bone masks.

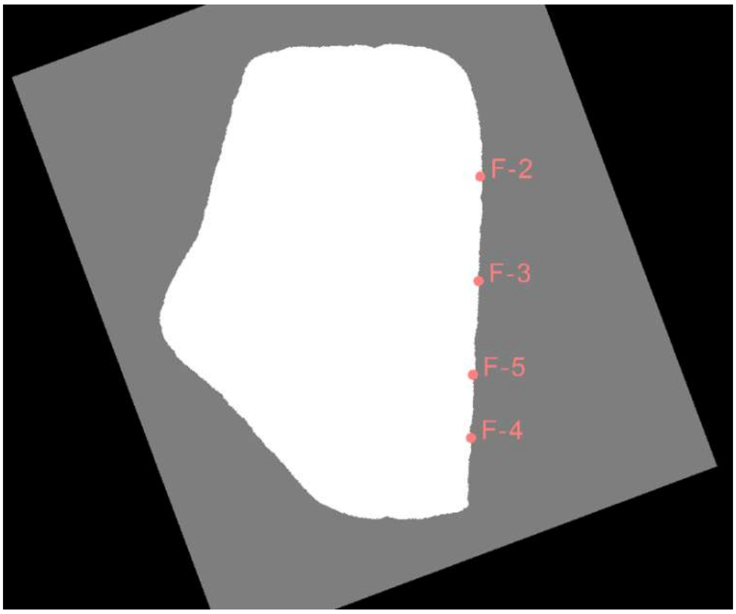

Figure 2.6: Example of the fiducial points along the surface line of the volar side of the radius in a centroidal transverse cut section.

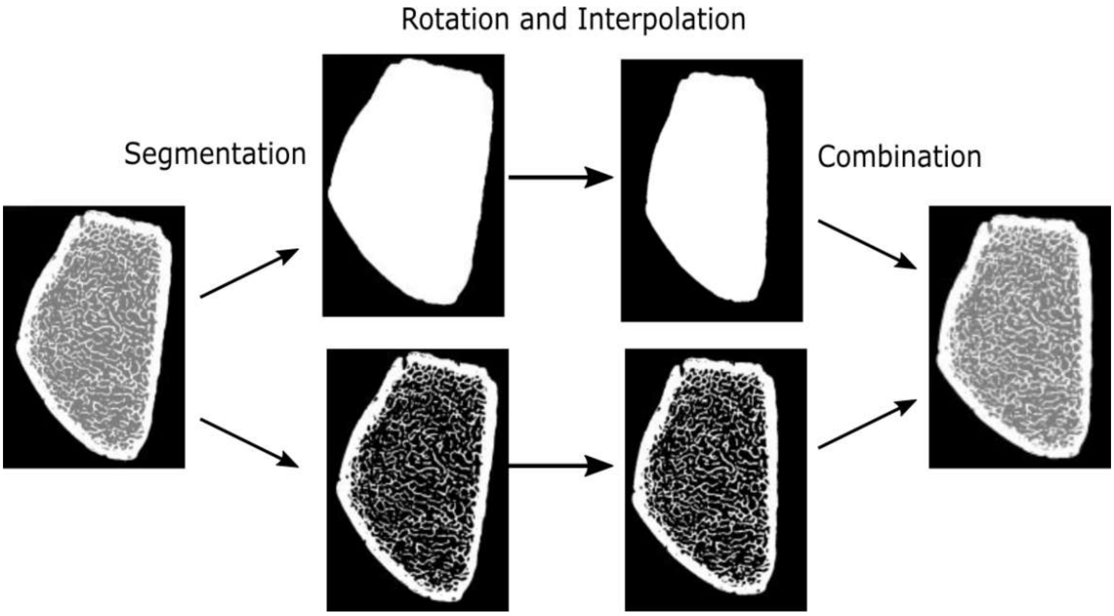

Figure 2.7: Segmentation of the bone image in two parts, which are then rotated and interpolated individually and recombined again.

The screw insertion depth was 10mm, this length was chosen in accordance with a previous study on volar locking plates [53]. Each bone image was then cropped to match the dimension of the screw image. The bone images were aligned so that the screw will be inserted 10mm into the bone (see Figure 2.8).

Finally, before virtually inserting the screw, a cylindrical mask was applied, to cut out the cylindrical volume of interest (VOI). The cylinder mask is a binary mask that is applied to a target image. The resulting image retains only those voxels of the original image where the cylinder mask had a gray value of one. The cylinder was created using Medtool and rotated to match the screw orientation. The diameter of the cylinder was set to the height of the radius section, i.e., 18mm. The cylinder mask was applied to both the segmented radius image and the masks of the radius image (Figure 2.8).

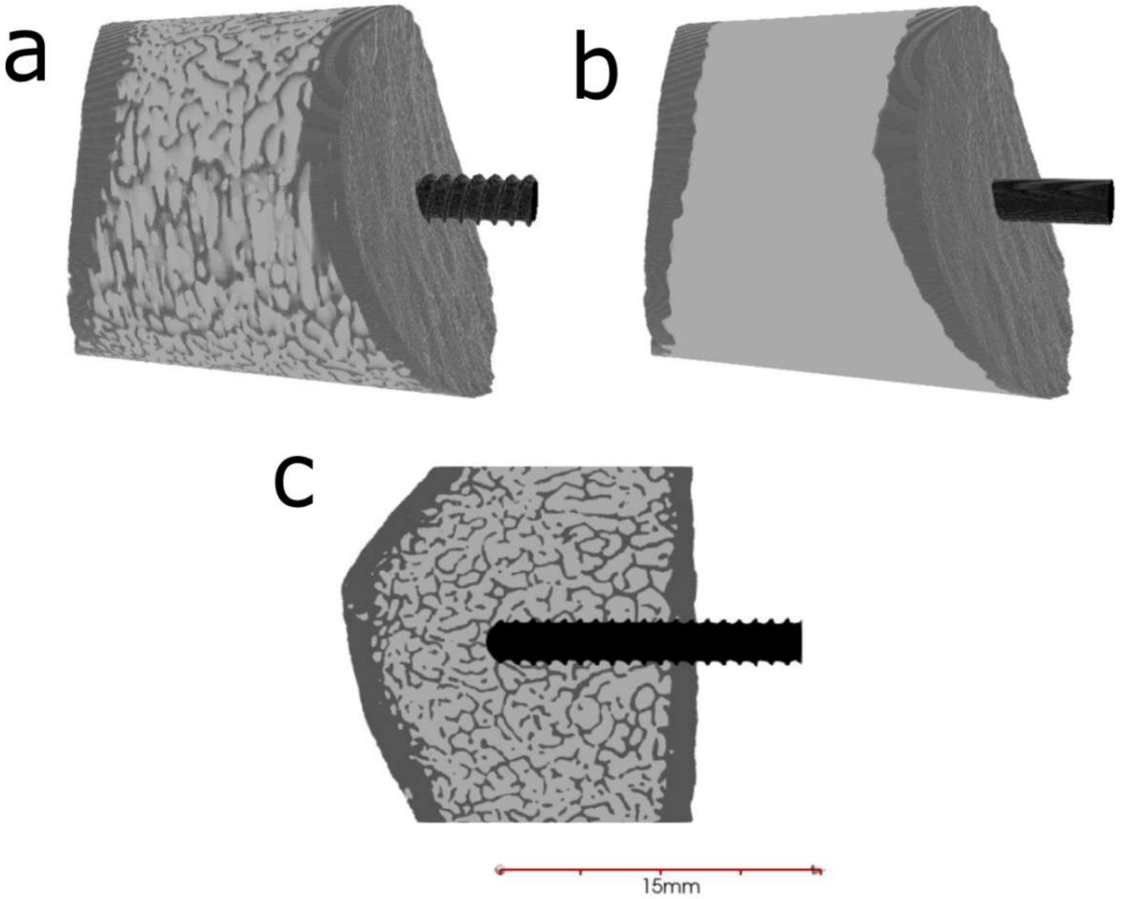

Figure 2.8: a) The final segmented image with the screw; b) The masked image with the cylinder; c) Cross-section of the segmented image with the screw

A boolean operation was applied to combine the screw image and the bone images. In that operation each voxel of the screw image that had a gray value of three replaced the gray value of the target image. That way, cylindrical bone samples with virtually inserted screws were created (see Figure 2.8). The same boolean operation was used for the the trabecular and cortical bone masks, but instead of using the screw image as input for the replacement, the cylinder image was used. The combined image is shown in Figure 2.8 b.

2.2.3 Morphometry

Quantitative morphometry is the usual method for describing bone architecture by calculating morphometric indices [54].
This information is valuable not only for homogenization, but also for the variability between specimens. It was shown that bone volume fraction (BV/TV) along with degree of anisotropy (orientation of structural elements) are significant indices of the mechanical properties of bone [54].
In order to assess the cortical and trabecular bone morphology, they had to be separated for each sample individually. The trabecular and cortical bone masks were used to extract the trabecular and cortical part individually. Multiplication with the radius image was applied to these extracted images and as a result the microstructure of the cortical as well as the trabecular part was obtained (see Figure 2.9).

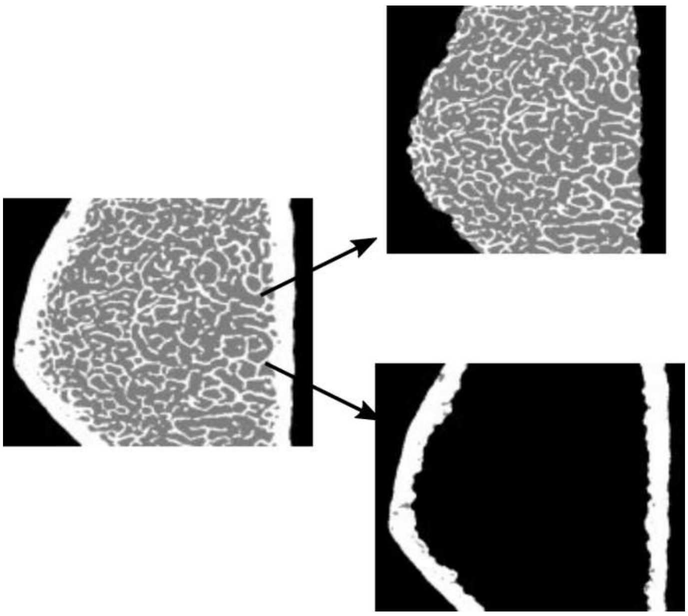

Figure 2.9: Preparation of bone images before assessment of bone morphometry

The chosen morphometric indices for the assessment of bone microstructure in Medtool were chosen in accordance with Bouxsein et al. [54]:

1. Trabecular bone volume/total volume (BV/TV)

ID	Tb. BV/TV (%)	Tb.Th (mm)	Tb.Sp (mm)	Tb.N ($\frac{1}{mm}$)	Ct.Th (mm)
179	0.26	0.22	0.59	1.07	1.24
182	0.14	0.19	0.88	0.50	0.94
186	0.25	0.24	0.69	0.92	1.08
189	0.23	0.24	0.71	0.85	1.06
193	0.21	0.22	0.76	0.73	1.02
195	0.19	0.19	0.64	0.81	1.20
196	0.10	0.18	0.98	0.87	0.86
200	0.14	0.23	0.97	0.52	0.83
203	0.24	0.32	0.96	0.87	0.78

Table 2.2: Morphometric indices for all samples: Trabecular relative bone density (BV/TV), mean trabecular thickness (Tb.Th), mean trabecular separation (Tb.Sp), mean trabecular number (Tb.N) and mean cortical thickness (Ct.Th)

2. Mean trabecular thickness
3. Mean trabecular separation
4. Mean trabecular number
5. Mean cortical thickness

Cortical thickness was obtained from images, containing only the volar cortical shell. The other morphometric indices were obtained from the trabecular images without a cortical shell. The resulting morphometric indices are shown in Table 2.2.

2.3 Finite Element Analysis

The aim of the FE analysis was the creation of μFE and hFE models of the screw-bone construct of each radius section and evaluating the stiffness and peri-implant SED in two different load cases.
Therefore, specimen-specific FE meshes based on CT data were necessary to generate the FE models.

2.3.1 μFE Modelling

Details are given in the following sections. In brief, μFE models were modeled with a screw and bone tissue, bone marrow and screw were modelled as isotropic and homogeneous materials. Material properties are listed in Table 2.3 and the model is shown in Figure 2.10. The bone-screw interface was assumed as fully osseointegrated, i.e., the nodes of the bone and the screw were assumed as fully tied.

The process of generating and solving the μFE models was the following:

1. Mesh generation
2. Creation of boundary conditions
3. Assigning material properties
4. FE model solving

Mesh Generation

The μFE models were created with Medtool and solved with ParOSol (2011, Cyril Flaig[50]). ParOSol is a fully-parallel μFE analysis code for solving large linear elasticity problems with high efficiency [55]. The voxel based mesh is generated directly in ParOSol from a 3D CT image and is based on a voxel geometry of the same size. The mesh size of the μFE models were 104 Mio.±17 Mio. elements with 312 Mio. degrees of freedom (DoF).

Creation of Boundary Conditions

The boundary conditions were defined as follows. The lateral surface nodes were constrained in all spatial directions (see Figure 2.10). All nodes that laid in a certain interval and bordered the gray values zero and three were the nodes for the lateral boundary conditions.

Assigning Material Properties

Bone, bone marrow and the inserted screw were assumed as linear elastic, isotropic. The screw was modelled as titanium alloy with E=115 GPa [38]. Bone marrow was included to capture the strains of the entire volume and for the accurate computation of volume averages. The material constants are listed in Table 2.3 [38][56].

Region	E(MPa)	$\nu(-)$
Bone marrow	1	0.3
Bone tissue	12000	0.3
Screw	115000	0.3

Table 2.3: Elastic material constants of bone, bone marrow and screw for the μFE model taken from [38][56]

FE Model Solving

Loads of the μFE model were applied as a force of 100 N on the surface nodes of the screw head in two load directions: one model with a pullout load in the x-direction and one model with a shear load in the negative z-direction (see Figure 2.10). Displacements, stresses, strains and strain energy densities of each element were selected as output parameters. Stresses and strains were evaluated at the centroid of each element. The models were solved with ParOSol.

2.3.2 hFE Modelling

Details are given in the following sections. In brief, bone material properties were extracted from the morphometric study and mapped onto the hFE mesh

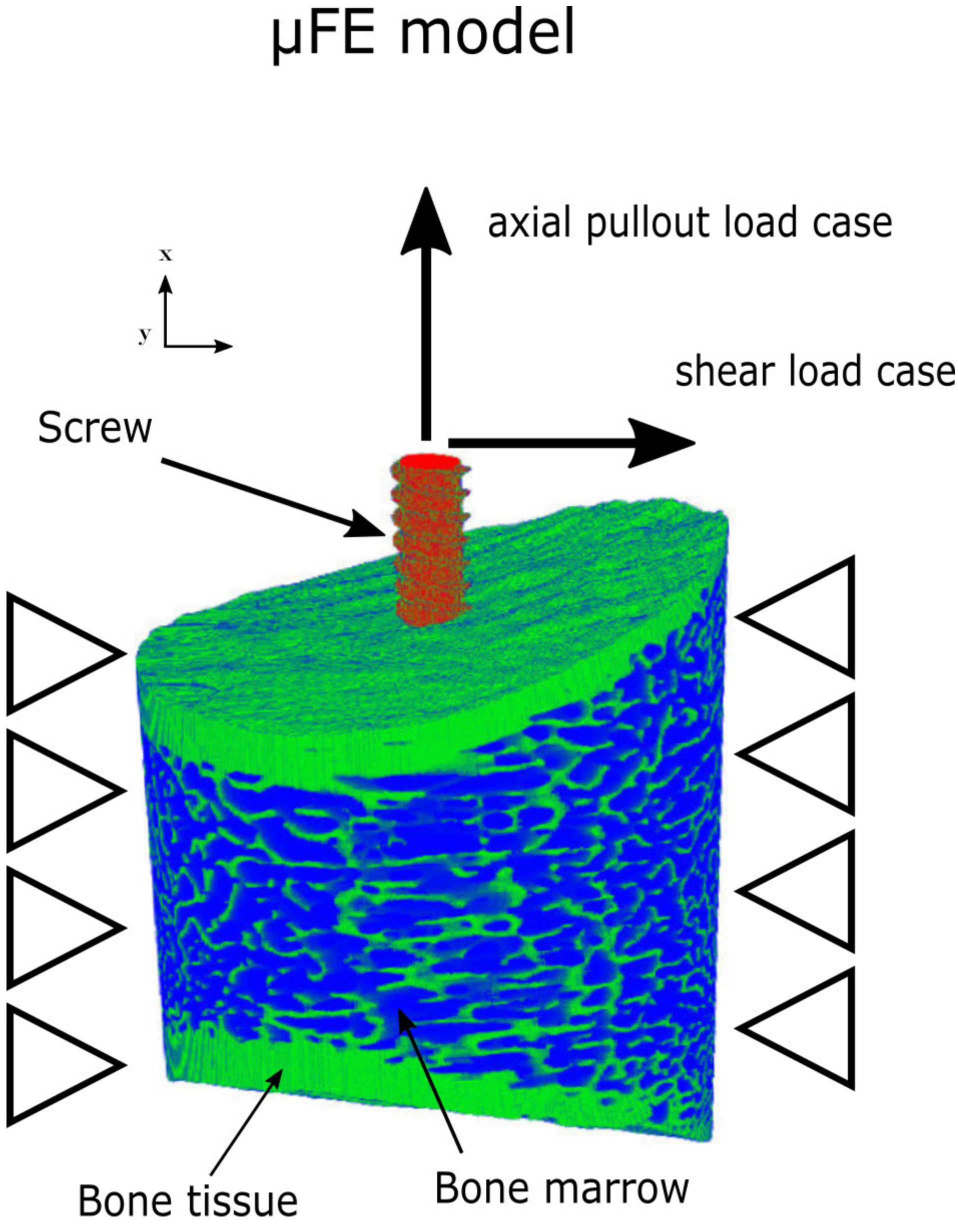

Figure 2.10: Lateral surface boundary conditions and applied load of the μFE model

elements. The final model was generated by imposing material properties, boundary conditions and load cases. The screw was simplified as an unthreaded cylinder. Material and boundary conditions for the hFE model are shown in Figure 2.14, Table 2.4 and Table 2.5. Cortical bone was modelled as isotropic and homogeneous material and trabecular bone was modelled as orthotropic and inhomogeneous material. A reference node was positioned in the center of the cylinder head and coupled with six degrees of freedom (DoF) to the most distal nodes of the cylinder (see Figure 2.14). All six DoF were unconstrained and a force of 100 N was applied on the reference node along two load directions.

The process of generating and solving the hFE models was the following:

1. Mesh generation
2. Mesh convergence study
3. Creation of boundary conditions
4. Assigning material properties
5. FE model solving

Mesh Generation

The mesh of the hFE models was created using the bone mask images with the virtually inserted cylinder (see Section 2.2.2 and Figure 2.8 b). The mesh was created with the built-in 3D-CGAL Mesher[57] in Medtool. This mesher generates 3D tetrahedron meshes of grayscale domains.
Two important parameters were defined for the mesh process: The *cell size* defines the size of a mesh tetrahedron and provides an upper limit for the circumradii of the tetrahedron. The *facet distance* is used for the approximation error of boundary and subdivision surfaces and influences the density of the mesh on curved surfaces. The resulting mesh was of the *.inp* data type, which is used by Abaqus as the input file format. The meshes of four-node linear tetrahedra (C3D4) were then converted to meshes of ten-node quadratic tetrahedra (C3D10) using Medtool. C3D10 elements were chosen for their superior mechanical and numerical behaviour in simulations, as previously reported by Maas et al. [58].

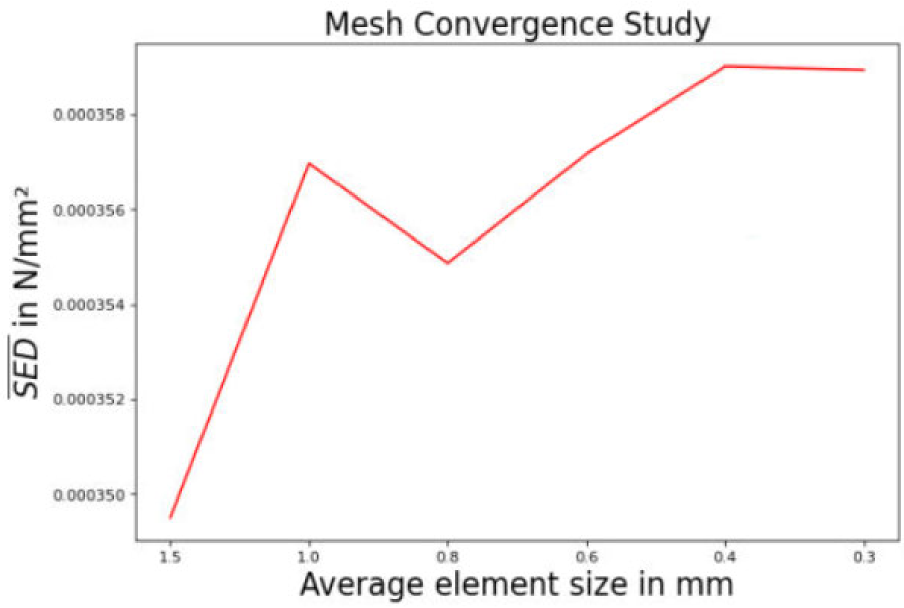

Figure 2.11: Mesh convergence study: Volume average SED in N/mm² within the model meshed in different sizes.

Mesh Convergence Study

The accuracy of a FE model depends on the mesh size. It is required to ensure a numerically correct solution independent of the mesh size. The mesh is considered sufficiently fine if the result of the target variable does not change outside predefined critical bounds if the mesh size is decreased [59]. Figure 2.11 shows the mesh convergence study with the the volume averaged SED as the chosen target variable. It was found that the change in average SED was less than 5 % relative to the finest mesh (0.3mm average element size) for any of the meshes tested (up to 1.5mm average element size).

However, a reduction in cell size and facet distance was necessary to eliminate geometric artefacts at the interface of the cylinder and the cortex of the samples (see Figure 2.12). Based on this finding and the results of the mesh convergence study a cell size of 0.4mm and a facet distance of 0.08mm were chosen as the mesh parameters.

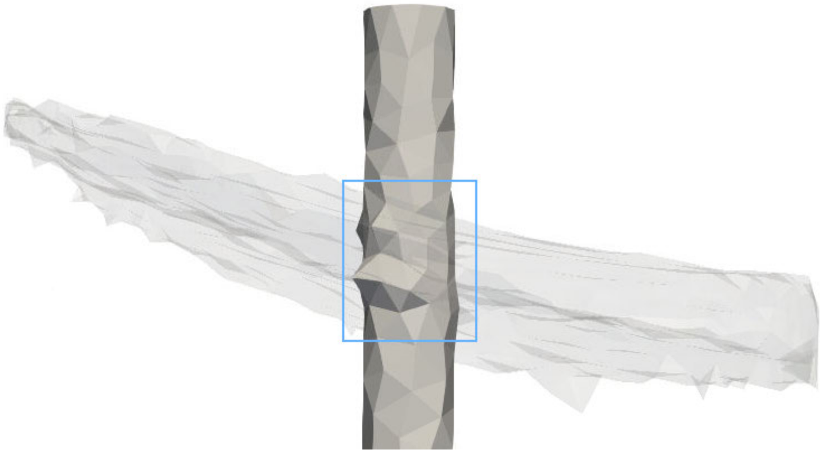

Figure 2.12: Tetrahedron spikes from the cylinder mesh on the interface between cortical and trabecular bone. Cortical bone is shown for reference here.

The mesh was further optimized using the 3D-CGAL Mesher optimization options, including a Lloyd-smoother, a sliver perturber and a sliver exuder [57].
The mesh size of the hFE models were 266095 $\pm$ 45491 elements with 0.8 Mio. DoF.

Creation of Boundary Conditions

The previously converted quadratic mesh was used as input for the *Medtool BC Generator*, which automatically creates nodesets of each boundary plane. The nodes of a mesh are assigned to different nodesets. Another node set was created to include all nodes on the lateral surface of the cylinder. A custom algorithm (2.2) was implemented to identify these nodes and add the nodeset to the hFE model. The nodes are shown in Figure 2.13. The boundary conditions were defined as follows: The lateral surface nodes were constrained in all spatial directions as shown in Figure 2.14. The surface nodes of the screw head were connected to a reference node.

Assigning Material Properties

The cortical bone was modelled as an isotropic homogeneous material with E=12 GPa and ν=0.3 [56]. E was chosen for consistency with the μFE material (E=12 GPa for bone tissue). The screw was modelled as titanium alloy with E=115 GPa

Algorithm 2.2: hFE Boundary Conditions
(Alexander Synek)

Input: All coordinates of the nodes of the model, physical inner and outer radius for cylinder
Output: Boundary nodes on cylinder surface appended to the Abaqus input file

Read input file and import all nodes and their coordinates
Capture the axis of the cylinder, including the start and end points
Calculate vectors from the origin to each node
Calculate vector projection and vector rejection
Filter nodes between inner and outer radius
Append nodes as a nodeset to the Abaqus input boundary condition file

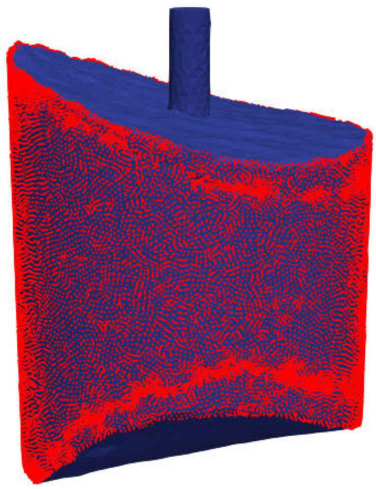

Figure 2.13: Captured lateral surface nodes for the boundary conditions on an exemplary hFE model based on the Algorithm 2.2

[38]. For the trabecular bone material, three different modelling strategies were implemented:

1. Isotropic homogeneous trabecular bone
2. Isotropic inhomogeneous trabecular bone
3. Orthotropic inhomogeneous trabecular bone

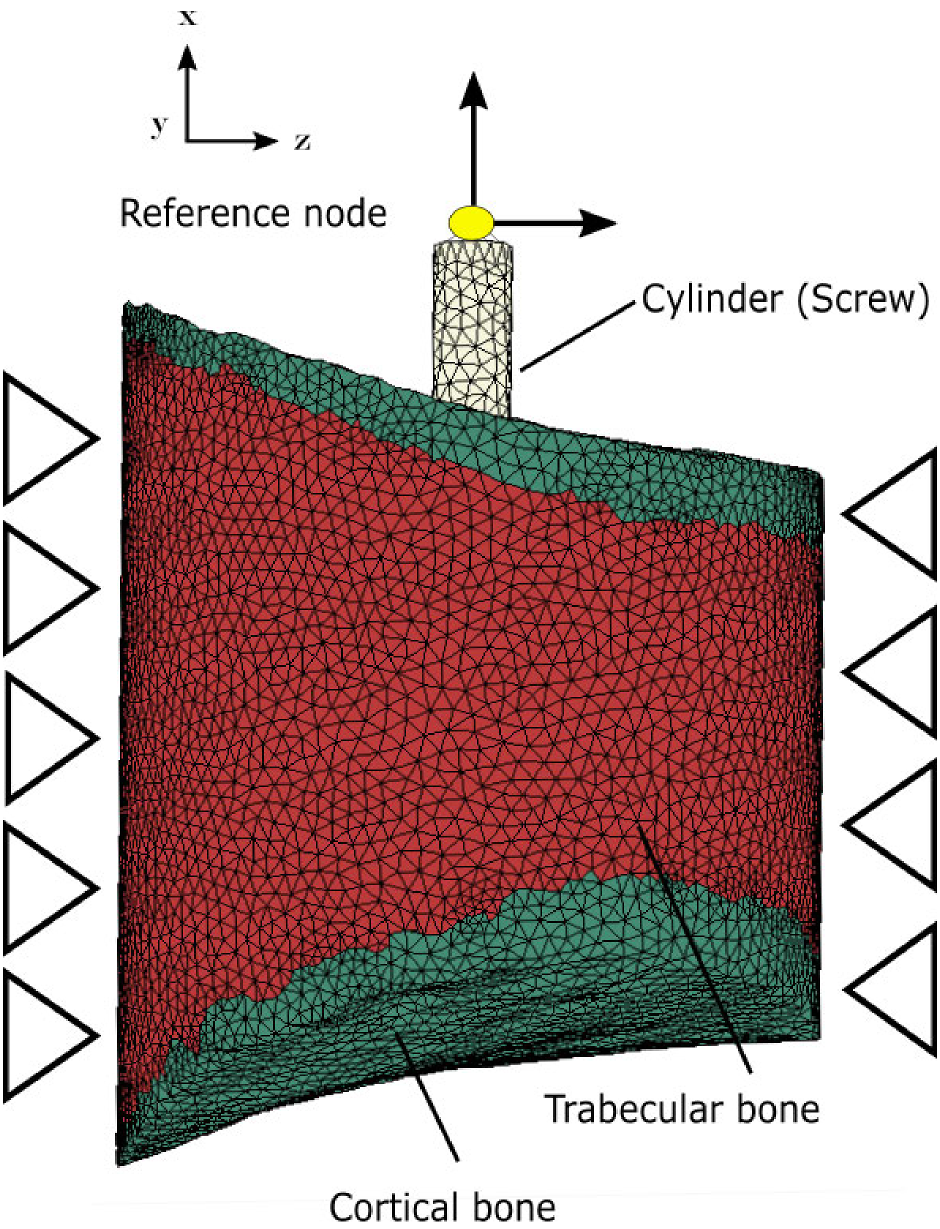

Figure 2.14: Lateral boundary conditions and reference node connected to the surface of the cylinder.

The elastic modulus associated with the trabecular region for the isotropic homogeneous case is based on the power law model in Equation 2.3 with given trabecular bone BV/TV (ρ) from the morphometric analysis (Section 2.2.3), Poisson ratio ν and the constants E_0 and k. The constants needed to define elastic behaviour of the cortical and trabecular bone and the screw are listed in Table 2.4 and are taken from [60].

$$E = E_0 \rho^k \tag{2.3}$$

Region	E_0(MPa)	ν_0(-)	k(-)	Symmetry	Homogeneity
Spongiosa	8813	0.24	1.63	Isotropic	Homogeneous
Cortex	12000	0.30	-	Isotropic	Homogeneous
Screw	115000	0.30	-	Isotropic	Homogeneous

Table 2.4: Elastic material constants of bone and screw (isotropic homogeneous, taken from [56, 38])

For the isotropic inhomogeneous and the orthotropic inhomogeneous properties of the trabecular bone, an automated material mapping algorithm by Pahr and Zysset[14] using Medtool was applied. The script performs multiple morphological analyzes on the CT images based on spherical region of interest (ROI) with a diameter of 7.5mm on a rectangular grid with 3.5mm spacing. The provided CT images for this algorithm were the previously created bone images without the cortical shell (see section 2.2.3 and Figure 2.9). The ROIs are automatically cropped and the fabric tensor and bone density for the bone structure are derived. These values are then interpolated for each element of the FE mesh based on the 3.5mm rectangular grid.
The input and output of the material mapping is shown in Figure 2.15 for an exemplary specimen.

Material cards that can be assigned are either

1. isotropic: a power law model based on BV/TV only
2. orthotropic: a density based fabric elasticity relationship based on BV/TV and fabric

For the orthotropic trabecular bone, a Zysset-Curnier type material model [61] was used:

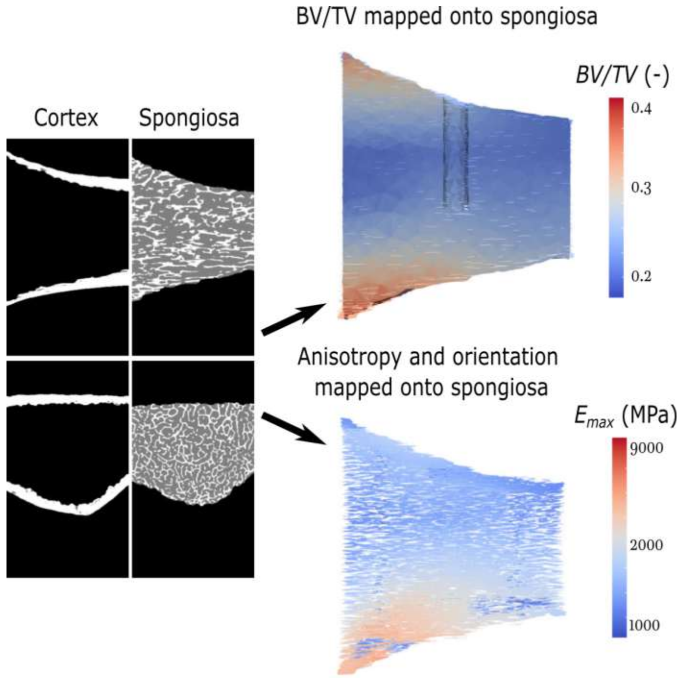

Figure 2.15: Exemplary results of the material mapping process: Right top: bone density mapped onto trabecular bone; right bottom: distribution of the maximum modulus of elasticity. The lines indicate the direction of the maximum elastic modulus (i.e., largest stiffness).

$$E_i = E_0 \rho^k (m_i^2)^l \quad \frac{E_i}{\nu_{ij}} = \frac{E_0}{\nu_0} \rho^k (m_i m_j)^l \quad G_{ij} = G_0 \rho^k (m_i m_j)^l \tag{2.4}$$

where E_i, G_{ij} and ν are elastic moduli, shear moduli and Poisson ratio that depend on the variable density ρ (=BV/TV) and fabric eigenvalues m_i, as well as the material constants E_0, k, l and G_0. For the isotropic models, the power law in Equation 2.3 was used.
The material constants of isotropic and orthotropic trabecular bone were taken from [56] and are listed in Table 2.5.

Note that orthotropic trabecular bone material was chosen as default. The main results of this study are therefore obtained using this type of material. A comparison of different trabecular material modelling strategies is presented at the end of the results section (Section 3.5). The finished hFE model is shown in Figure 2.16.

Region	E_0 (MPa)	ν_0(-)	k(-)	G_0 (MPa)	l(-)	Symm.	Homogeneity
Spongiosa	10320.40	0.22	1.62	3470.70	1.10	Ortho.	Inhom.
Spongiosa	8813.00	0.24	1.63	-	-	Iso.	Inhom.
Cortex	12000.00	0.3	-	-	-	Iso.	Hom.
Screw	115000.00	0.3	-	-	-	Iso.	Hom.

Table 2.5: Elastic material constants of bone and screw (isotropic and orthotropic inhomogeneous), taken from [56]

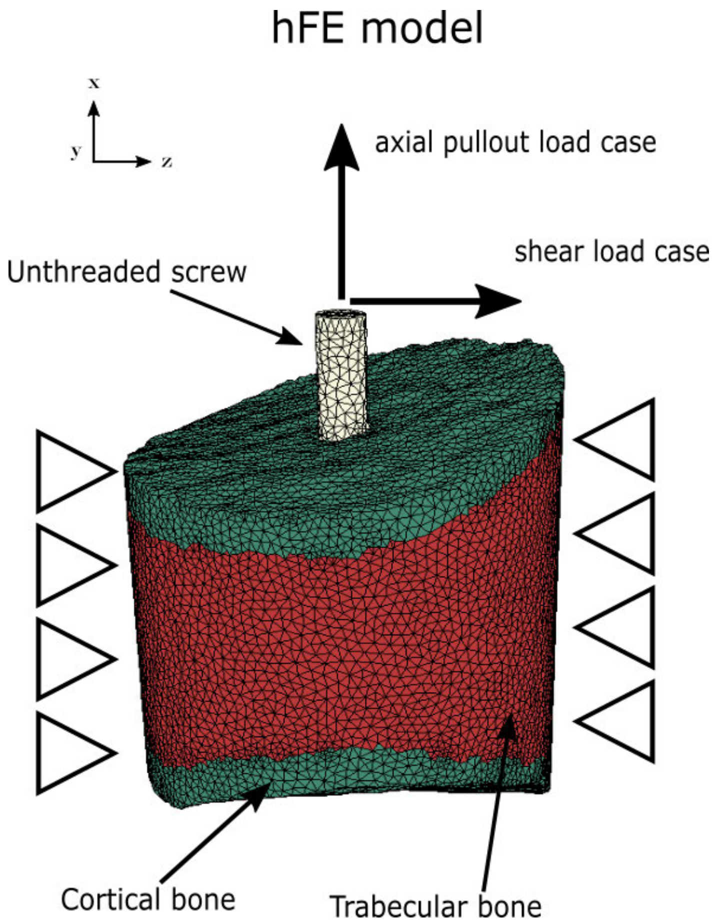

Figure 2.16: Finished hFE model

FE Model Solving

A force of 100 N was applied on the reference node in two loading directions: one model with a pullout load in the x-direction and one model with a shear load in the negative z-direction (see Figure 2.14).
Displacements at the reference node, strain energy densities and coordinates of the centroid of each element were chosen as output variables. The models were solved using Abaqus 2021.

2.4 Data Processing and Evaluation

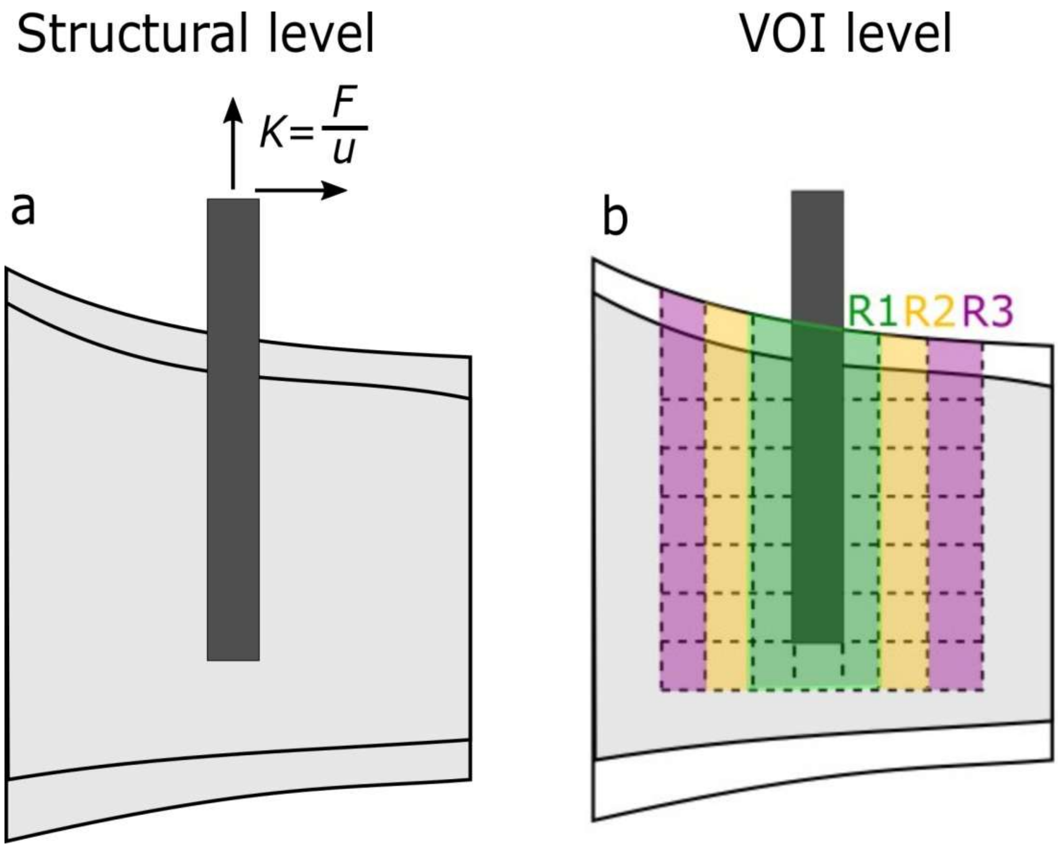

Figure 2.17: Two levels of comparison: Structural stiffness of the whole model and volume average SED with three different sizes (Radius $R1$, $R2$ and $R3$)

The resulting data was evaluated and compared at two assessment levels. At the structural level, the spring stiffnesses of the model were evaluated based on Equation 2.5 (see Figure 2.17 a). The spring stiffness K was defined as the ratio of the total nodal force F and the nodal displacement u (see Equation 2.5). The spring stiffness of the hFE models were calculated based on forces and displacements of the reference node in their respective load directions. The spring stiffness of the μFE models were calculated from forces and averaged displacements of the surface nodes of the screw head.

$$K = \frac{F}{u}(\text{in N/mm}) \tag{2.5}$$

μFE and hFE spring stiffness were compared against each other for all specimens by the use of linear regression [62]. It describes a relation between two or more variables by fitting a linear equation to the data by using the least squares approach. Additionally the coefficient of determination (commonly known as r^2) was calculated to quantify the strength of the association. The r^2-value is represented by a value between 0.0 and 1.0, where a value of 1.0 shows a perfect fit (i.e., no residuals). However, note that even though the goodness of fit may be 1.0, a 1:1 relation of the two methods is not guaranteed. This is only the case if the regression line has a slope of one and an intercept of zero. For that reason, the results were also compared graphically by plotting the perfect relation (x=y) and comparing the data points and the fitted regression line to this 1:1 fit.
Additionally, Bland-Altman plots are plotted to show systematic measurement errors [63]. It plots the difference and mean between the two measurement methods. The plot shows three lines indicating the mean of the difference and the mean of the difference $\pm 1.96 \cdot \sigma$ (σ=standard deviation of the difference).

The second level of assessment was the cylindrical volume of interest. A radius of 3mm was chosen for the VOI and divided into three radii $R1$, $R2$ and $R3$, each 1mm thick (as seen in Figure 2.17 b). The length of the VOI has been increased by 2mm past the tip of the screw. The same consideration was used in a previous study on volar plate fixations of distal radius fractures [64]. The variable of interest for this level was the strain energy density (SED), which is given by

$$SED = \frac{1}{2}\epsilon_{ij}\,\sigma_{ij} \tag{2.6}$$

where ϵ_{ij} are the components of the strain tensor $\underline{\underline{\boldsymbol{\epsilon}}}$ and σ_{ij} are the components of the stress tensor $\underline{\underline{\boldsymbol{\sigma}}}$ [65]. The SED was chosen to investigate if the volume average elastic energy density in the peri-implant bone of the μFE model (microscropic scale) is consistent with that of the hFE model (macroscopic scale). It was chosen especially, because in the case of a RVE the boundary conditions are defined such that the Hill-Mandel condition is kept, preserving the energy consistent equivalence between the two scales, meaning the average of microscopic strain energy density (SED) is the same as the macroscopic SED [33]. Volume averaged strain energy densities (SED) were computed and compared between hFE and μFE models for each sample for the three VOI sizes. To calculate the volume averaged SED, the volume had to be calculated for each tetrahedron ($V_{\mathrm{tet,i}}$) and multiplied by the SED at the element centroid ($SED_{\mathrm{tet,i}}$). The sum of these results was divided by the total volume (V_{total}) (see Equation 2.7, where i denotes the element inside the ROI, N the number of elements in the ROI and $\overline{SED}$ the volume averaged strain energy density). The classification of the elements in the different ROIs was based on the centroid of the element located in the ROI.

$$\overline{SED} = \frac{\sum_{i=1}^{N} SED_{\mathrm{tet,i}} \cdot V_{\mathrm{tet,i}}}{V_{\mathrm{total}}} \tag{2.7}$$

In addition to the two main results (structural stiffness and volume averaged SED), SEDs were also compared at the meso scale for one sample to test the influence of the material mapping strategy. Zones on the meso scale of at least $1\mathrm{mm}^3$ in size were compared. Volume averaged strain energy densities of these zones were compared and evaluated between hFE and μFE models for one sample. The subdivision of these zones is as follows: 1mm high slices divided into three VOI sizes, each quartered. A transverse view is shown in Figure 2.18. Cortical and trabecular bone were separated for all comparisons except the structural level. The cortical shell was only separated into three VOI and quartered but not sectioned in 1mm high slices. The cylindrical VOI of a sample is shown in Figure 2.19.
The influence of morphometry on the volume averaged SED is shown in section

3.4. and the influence of the material mapping is shown in section 3.5. For these comparisons the whole VOI size was considered (VOI size $R3$). A custom written script in Python was used to evaluate the two levels.

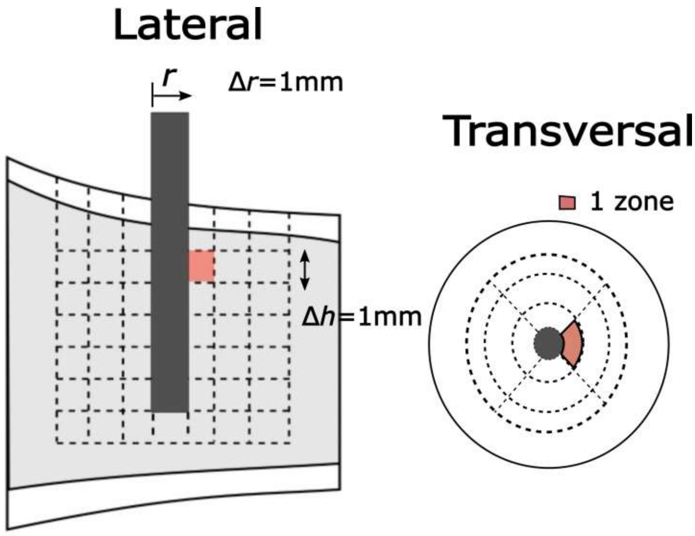

Figure 2.18: Transverse view of the subdivision in several zones at the meso scale (~1mm³) used to compare SEDs predicted by hFE and μFE locally.

Figure 2.19: Cylindrical VOI of the hFE model approach

2.5 Hardware and Computational Time

Both hFE and μFE models were solved on a system with an AMD EPYC 7542 32-Core CPU and 64 GB of RAM.
The hFE models were solved with Abaqus 2021 on 16 CPUs. The mesh size of the hFE models were 266095 ± 45491 elements with 0.8 Mio. DoF.
The μFE models were solved with ParOSol [50] on 32 CPUs. The mesh size of the μFE models were 104 Mio.$\pm$17 Mio. elements with 312 Mio. DoF.
Table 2.6 shows the average model solving time for both models in both load cases.

Model and load case	Min (s)	Max (s)	Mean (s)
hFE axial pullout	652	1508	864
hFE shear	660	1320	867
μFE axial pullout	1551	42386	13872
μFE shear	1029	42371	8250

Table 2.6: Results of the computation time of the FE analysis (Wall clock time)

CHAPTER 3

Results

The results are structured in accordance to the graphical abstract (Figure 2.1). First, the comparison between μFE and hFE models based on deformation and the spring stiffness is presented. Then a qualitative comparison of the peri-implant SED is shown and the peri-implant volume average SED are compared quantitatively between the FE model types. Finally, the influence of material mapping for trabecular bone and the influence of the morphometric parameters on predicted volume average SEDs is presented.

3.1 Deformation

The displacement fields were qualitatively similar for both load cases between hFE and μFE models (Figure 3.1). In both models, the deformations in the shear load case were larger than in the axial pull out load case.

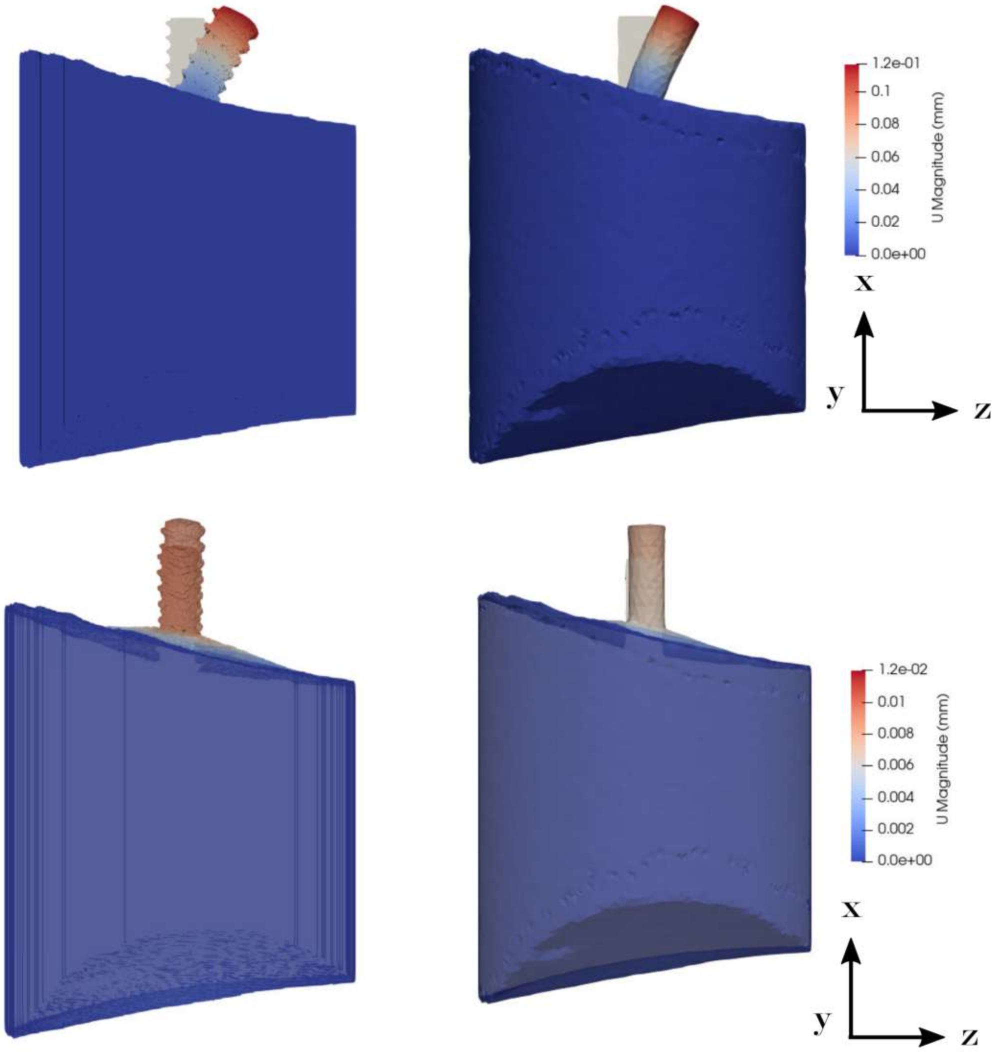

Figure 3.1: Displacement field magnitudes plotted for the hFE and μFE model for both load cases. Top row: shear load case; bottom row: axial pullout load case

3.2 Stiffness

The results of the linear regression analysis comparing μFE and hFE spring stiffness for the axial and shear load cases is shown in Figure 3.2 and Figure 3.3, respectively. The hFE models consistently overestimated the stiffness predicted by the μFE models (30% on average for axial pullout; 18.7 % on average for shear).

Model and load case	Min (N/mm)	Max (N/mm)	Mean (N/mm)	SD (N/mm)
hFE axial pullout	3668.38	12293.65	8459.03	3077.91
hFE shear	671.73	915.22	795.77	88.07
μFE axial pullout	2035.37	10061.96	6314.23	2926.01
μFE shear	509.74	782.35	659.77	100.79

Table 3.1: Descriptive statistics of the computed uniaxial stiffness for both model approaches and their respective load cases: minimum, maximum, mean and standard deviations

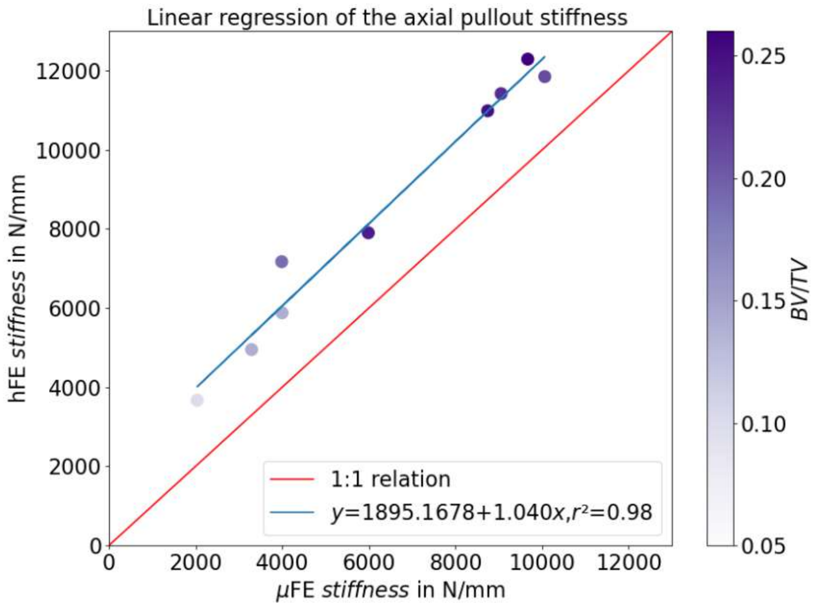

Figure 3.2: Linear regression of the spring stiffness in the axial pullout load case. The statistics of the linear regression is presented in the legend: Intercept, slope and the coefficient of determination (r^2). A 1:1 line is drawn in red to show an ideal relation. The color scale indicates the trabecular bone volume fraction (BV/TV) of each specimen.

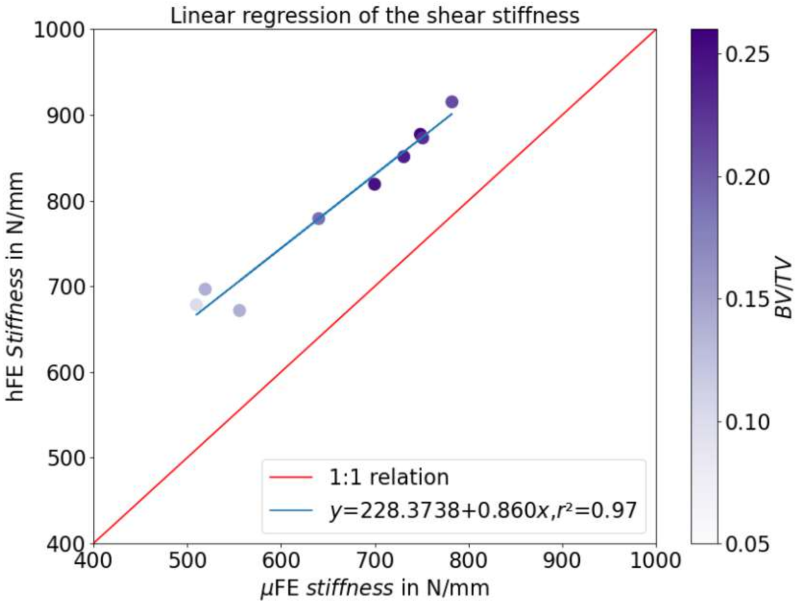

Figure 3.3: Linear regression of the spring stiffness in the shear load case. The statistics of the linear regression is presented in the legend: Intercept, slope and the coefficient of determination (r^2). A 1:1 line is drawn in red to show an ideal relation. The color scale indicates the trabecular bone volume fraction (BV/TV) of each specimen.

The calculated stiffness of all hFE models in both load cases were higher than the stiffness calculated from the μFE models. The axial stiffness correlated well between the two methods ($r^2 = 0.98$, $p < 0.0001$, see Figure 3.2), and the slope of the regression line was close to one, indicating almost 1:1 agreement. However, the intercept showed a mean offset of 1895.17N/mm, indicating that the hFE model approach overestimated the stiffness of the μFE model.
The shear stiffness correlated well between the two methods ($r^2 = 0.97$, $p < 0.0001$ see Figure 3.3), despite the lack of a 1:1 agreement with a regression line of 0.86. All hFE models in the shear load case overestimated the stiffness of the μFE model by a mean offset of 228.37N/mm.
Axial pullout stiffness was roughly ten times larger than shear load stiffness (Table 3.1). Bland-Altman plots for both load cases are shown in Figure 3.4. In the case of axial pullout the difference between μFE and hFE increased very slightly with

increasing stiffness values (Figure 3.4). Specimen *195* showed a higher difference compared to specimens in the same range of mean stiffness.
On the contrary, stiffness differences appeared larger for lower stiffnesses in the shear load case. Specimens *196* and *200* showed a high difference in stiffness.
In both load cases, higher bone density lead to larger stiffness and the difference between μFE and hFE predicted stiffness appeared to be unrelated to the bone density (Figure 3.2, 3.3).

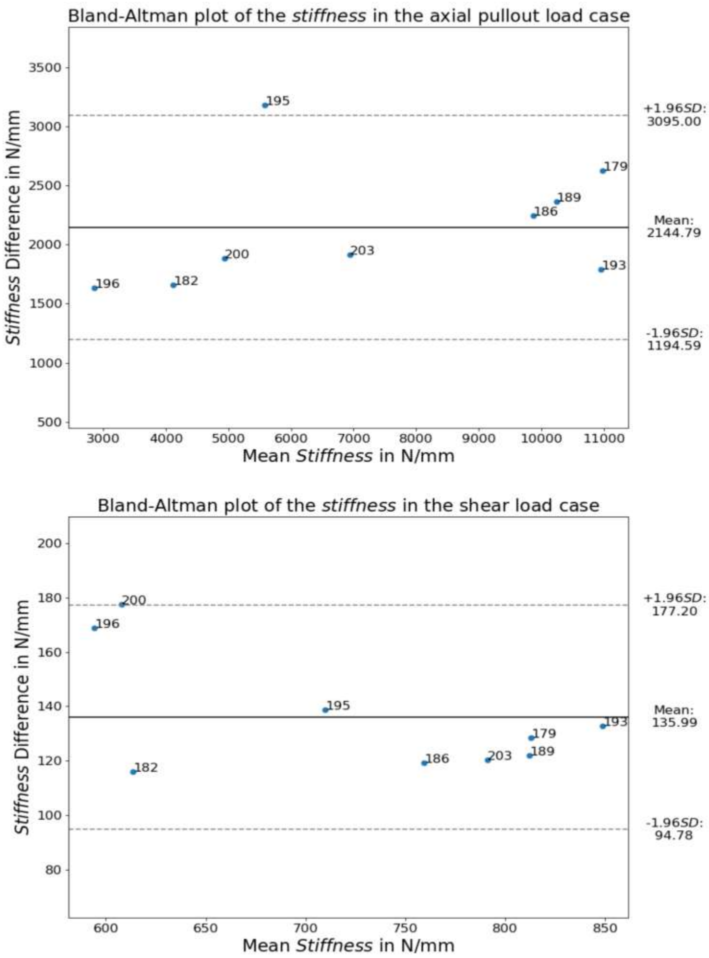

Figure 3.4: Bland Altman plot of the spring stiffness in the axial pullout and shear load case

3.3 Peri-implant SEDs

This section shows a qualitative comparison of the peri-implant SEDs and a comparison of the volume averaged peri implant SEDs.

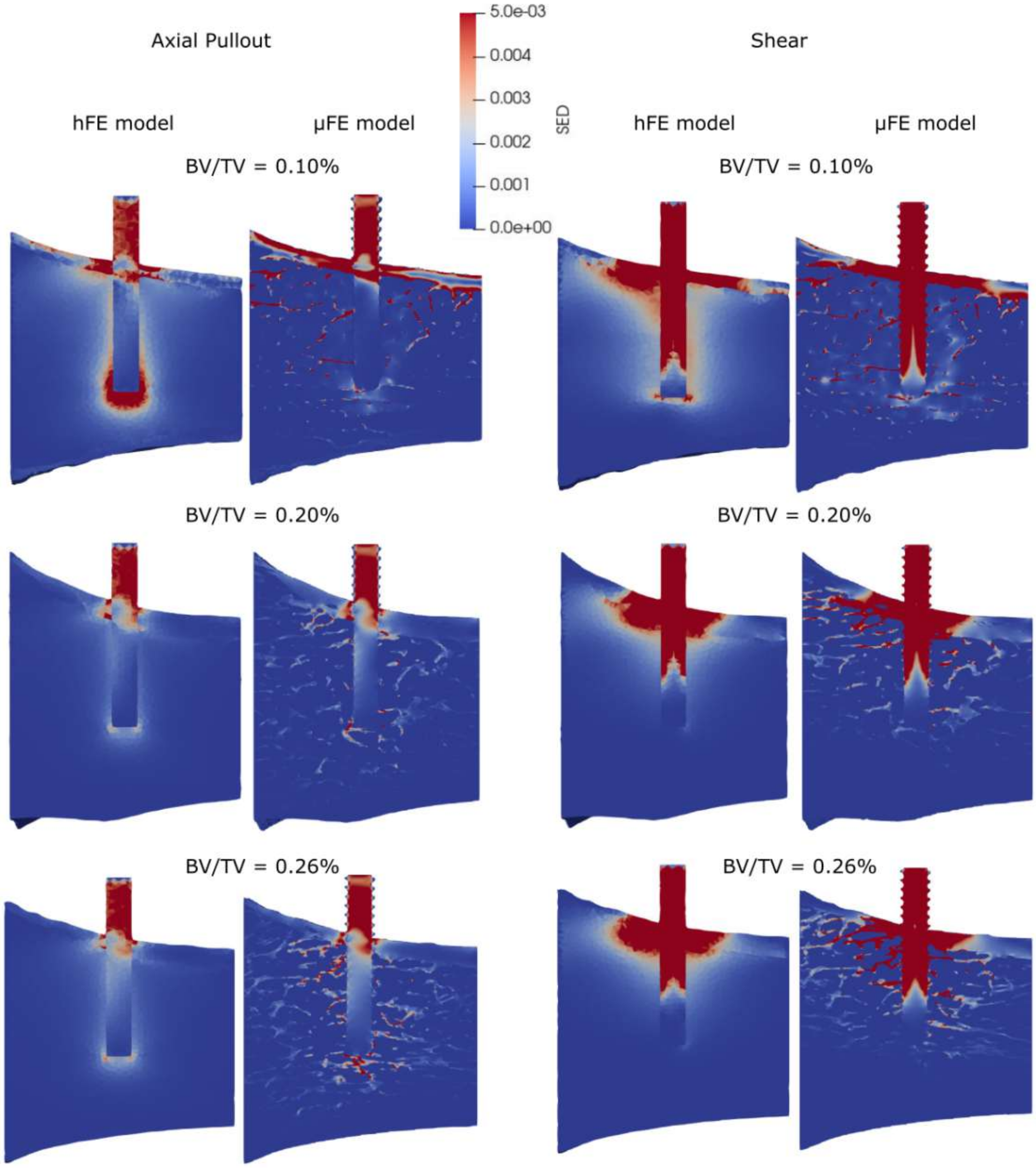

Figure 3.5: The SED distribution of both FE models in cross section for different trabecular BV/TV

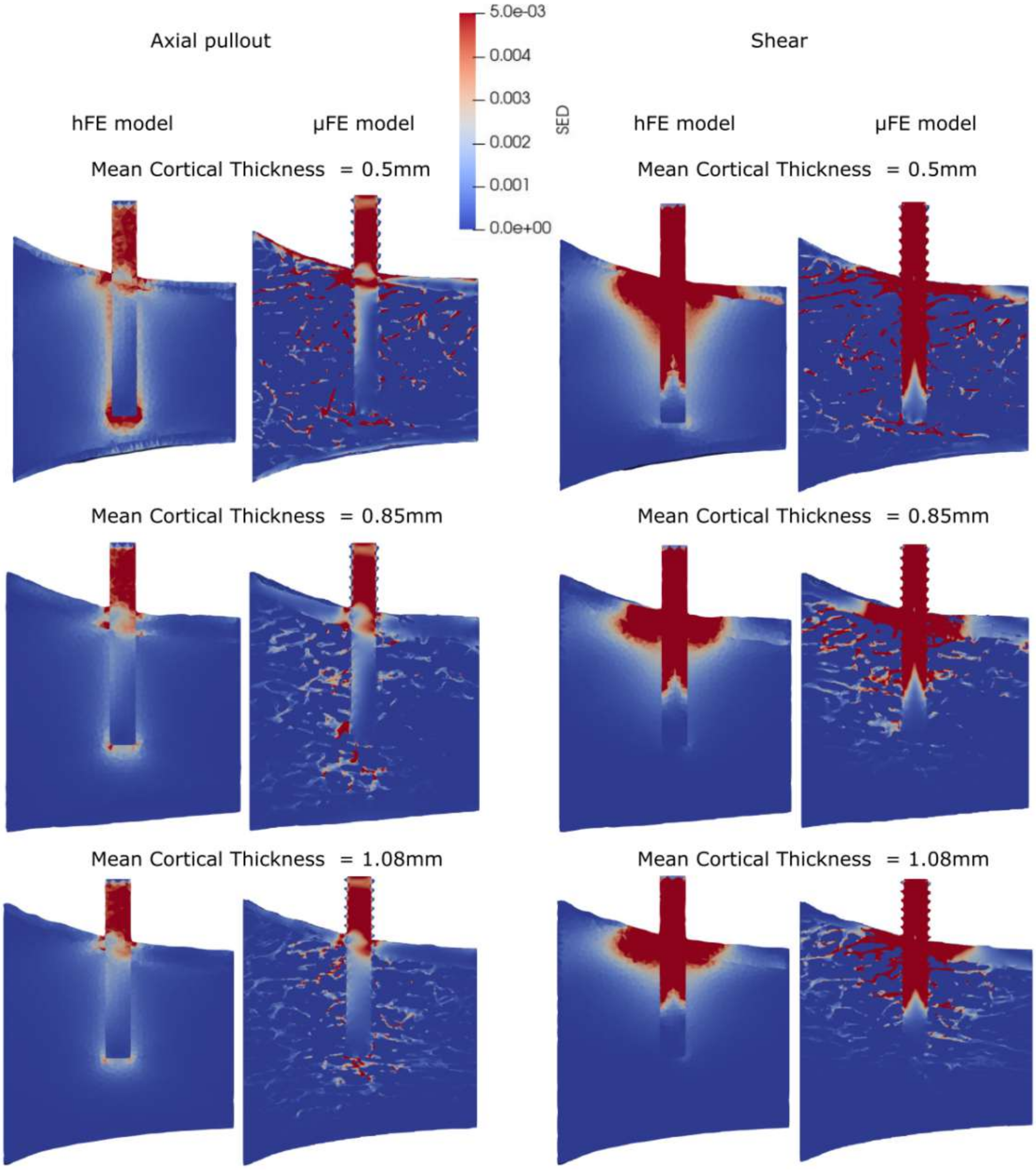

Figure 3.6: The SED distribution of both FE models in cross section for different cortical thicknesses

Figure 3.5 and Figure 3.6 show a qualitative comparison of the local SED distribution for increasing trabecular BV/TV and increasing cortical thickness, respectively. The similarities of the two modeling approaches in predicting general trends of SED distributions within the bone sample was presented. However, SED distributions appeared to deviate between μFE and hFE model particularly in the trabecular bone regions. Local peaks in the trabecular region were essentially averaged-out in the hFE models.

The volume averaged SED correlated well between the two models in the axial pullout load case ($r^2 = 0.96$, $p < 0.0001$ see Figure 3.7), despite the lack of a 1:1 agreement. Lower average SEDs were observed for larger VOI sizes. This could be explained by the high SEDs in close proximity to the screw, which are averaged-out as the VOI size increases. However, all three VOI sizes showed a similar correlation pattern. The SED in the μFE model was higher than in the hFE model for all VOI sizes. Lower bone density generally led to higher volume averaged SEDs (Figure 3.7, 3.8).

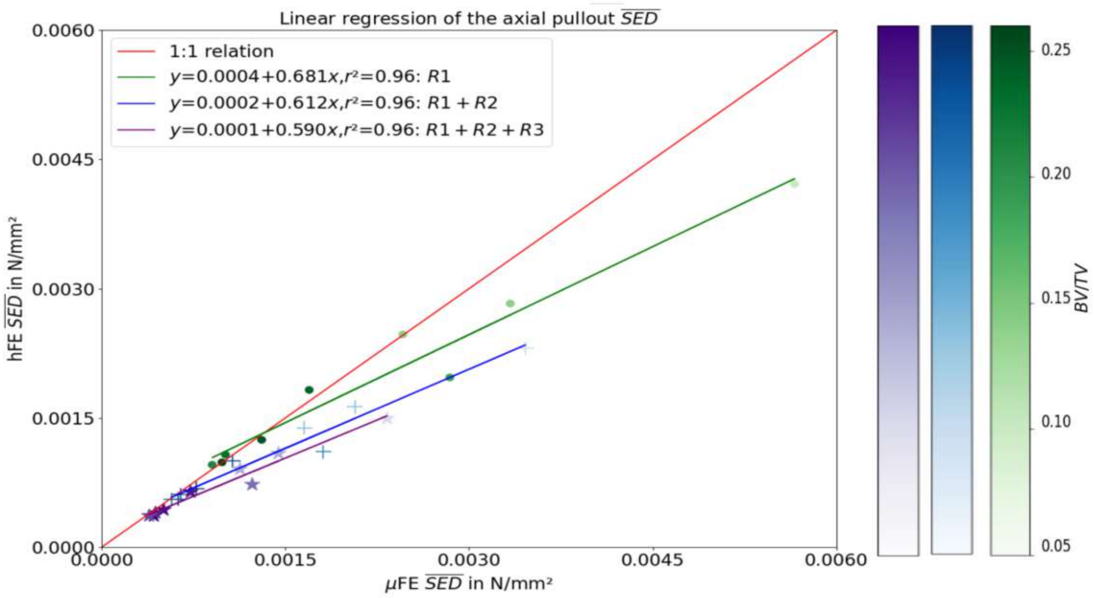

Figure 3.7: Linear regression of the volume averaged SED of the axial pullout load case. The statistics of the linear regression for all three radii are presented in the legend: Intercept, slope and the coefficient of determination (r^2). A 1:1 line is drawn in red to show an ideal relation. The three radii of the cylindrical volume of interest (VOI) $R1$, $R2$ and $R3$ are indicated in the colors green, blue and purple and in markers dot, plus and star. The color scale indicates the trabecular bone volume fraction (BV/TV) of each specimen.

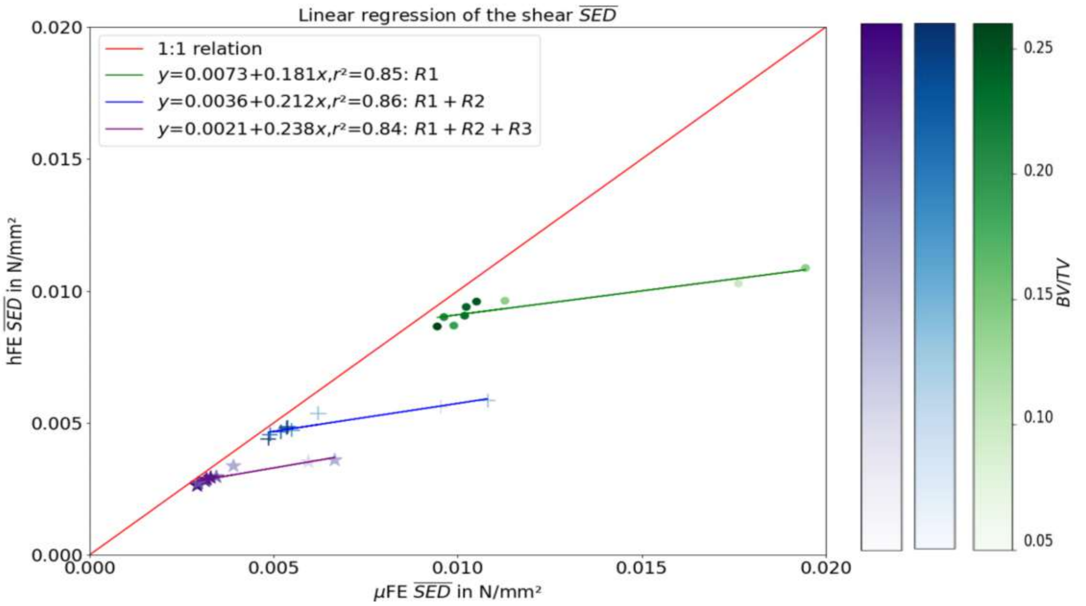

Figure 3.8: Linear regression of the volume averaged SED of the shear load case. The statistics of the linear regression for all three radii are presented in the legend: Intercept, slope and the coefficient of determination (r^2). A 1:1 line is drawn in red to show an ideal relation. The three radii of the cylindrical volume of interest (VOI) $R1$, $R2$ and $R3$ are indicated in the colors green, blue and purple and in markers dot, plus and star. The color scale indicates the trabecular bone volume fraction (BV/TV) of each specimen.

The volume averaged SED in the shear load case correlated well between the two methods ($r^2 = 0.84$, $p < 0.0004$, see Figure 3.8), but the slope of the regression line was close to 0.2, indicating a weak agreement. Furthermore, all hFE models underestimated the volume averaged SED of the μFE model in all three VOI sizes. Two specimens showed considerably higher volume average SED in the μFE model than the others.

Figure 3.9 shows Bland-Altman plots for both load cases. At low mean SED the difference was close to zero meaning good accordance for both load cases. In the shear load case the difference for the specimens *196* and *200* were very high, which is in accordance to the two specimens in the linear regression of the shear load case.

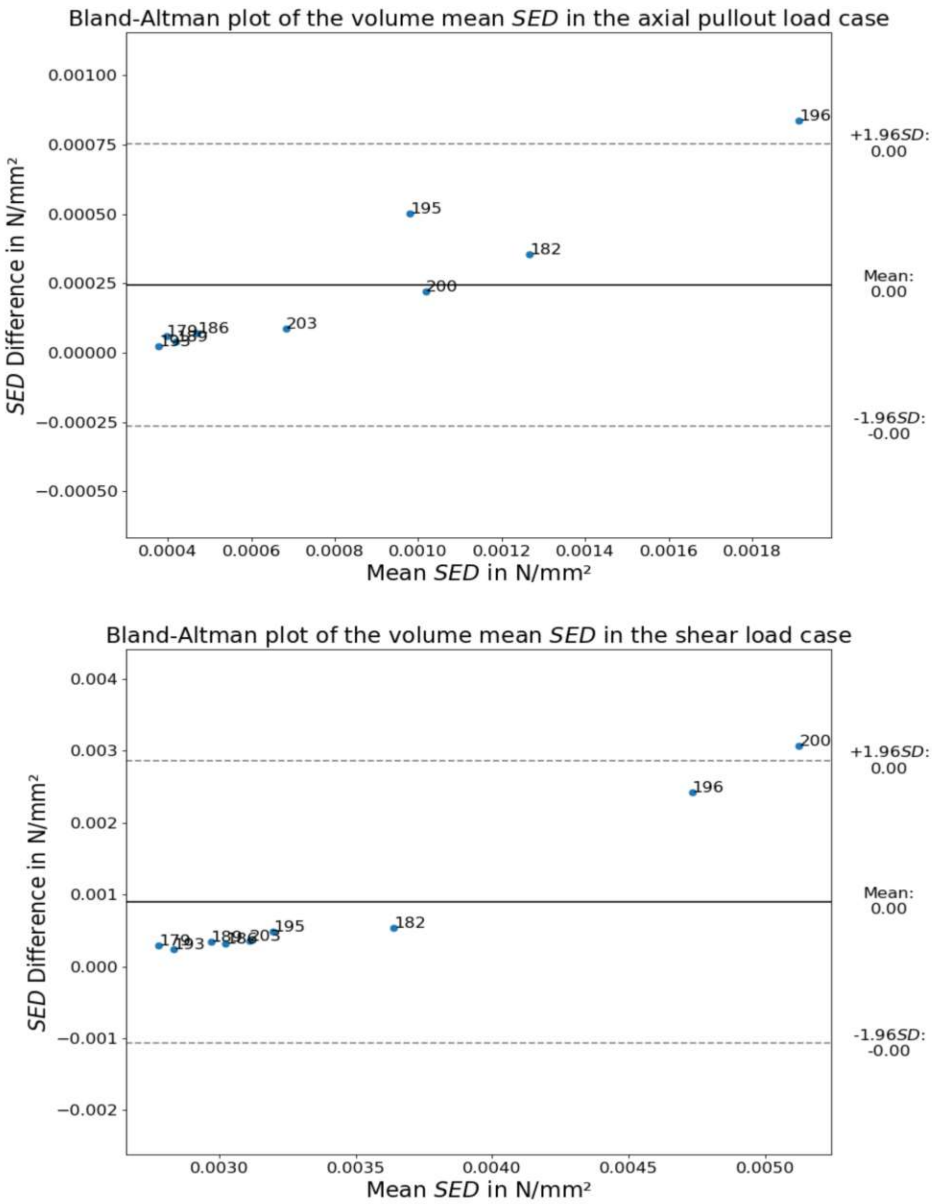

Figure 3.9: Bland Altman plot of the volume averaged SED in the axial pullout and shear load case

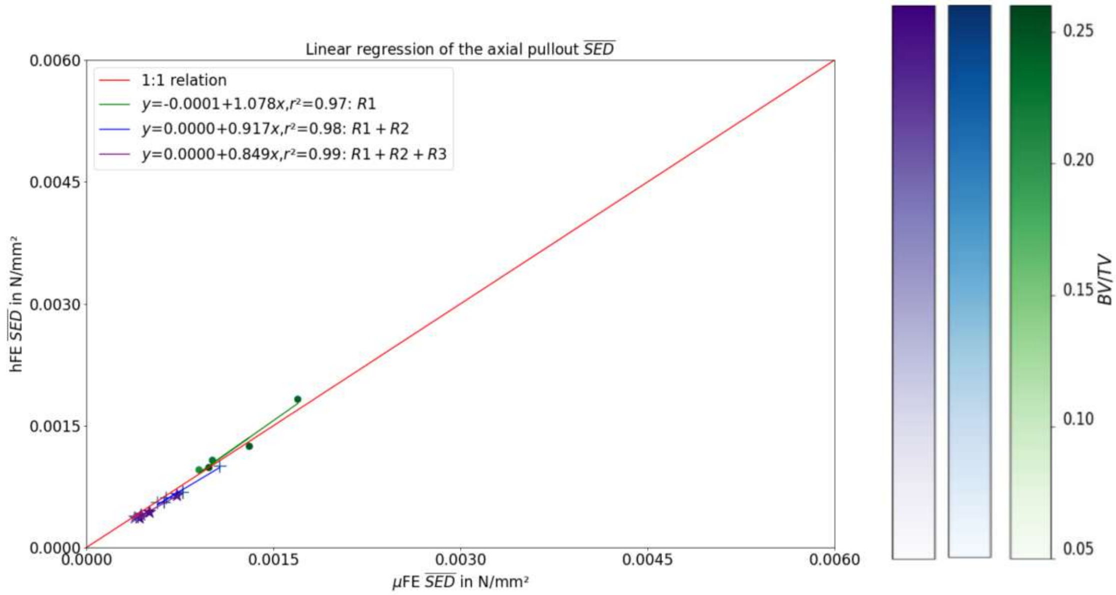

Figure 3.10: Linear regression of the volume averaged SED of the axial pullout load case with samples with a trabecular BV/TV greater than 20%. The statistics of the linear regression for all three radii are presented in the legend: Intercept, slope and the coefficient of determination (r^2). A 1:1 line is drawn in red to show an ideal relation. The three radii of the cylindrical volume of interest (VOI) $R1$, $R2$ and $R3$ are indicated in the colors green, blue and purple and in markers dot, plus and star. The color scale indicates the trabecular bone volume fraction (BV/TV) of each specimen.

Since a trend was observed that lower BV/TV resulted in larger errors, the regression analyses were repeated including only samples with trabecular BV/TV above 20%. If only specimens with a trabecular BV/TV greater than 20% were considered, the correlation of volume averaged SED in the axial pullout load case increased slightly from $r^2 = 0.96$ to $r^2 = 0.97$ and a 1:1 agreement was reached 3.10.
In the shear load case, the correlation of the volume averaged SED also increased from $r^2 = 0.84$ to $r^2 = 0.85$ with samples of trabecular BV/TV greater than 20%. Furthermore, the slope of the regression line increased from 0.20 to 0.74, indicating stronger agreement compared to the case where samples with lower trabecular BV/TV were included.

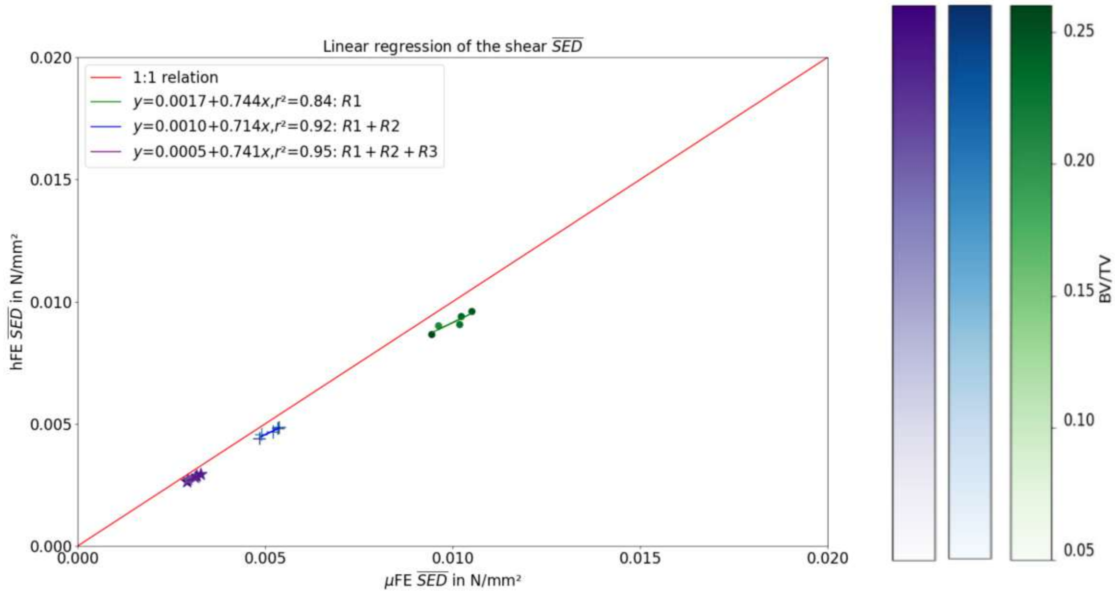

Figure 3.11: Linear regression of the volume averaged SED of the shear load case with samples with a trabecular BV/TV greater than 20%. The statistics of the linear regression for all three radii are presented in the legend: Intercept, slope and the coefficient of determination (r^2). A 1:1 line is drawn in red to show an ideal relation. The three radii of the cylindrical volume of interest (VOI) $R1$, $R2$ and $R3$ are indicated in the colors green, blue and purple and in markers dot, plus and star. The color scale indicates the trabecular bone volume fraction (BV/TV) of each specimen.

3.4 Influence of Morphometry

This section will show the influence of morphometric indices on the volume averaged SED for the specimens.
The difference in volume averaged SED between μFE and hFE were compared against five different morphometric indices of trabecular and cortical bone: trabecular BV/TV, cortical thickness and mean trabecular thickness are shown in Figure 3.12; mean trabecular separation and mean trabecular number are shown in Figure 3.13.
In both load cases, samples with bone density below 20% trabecular BV/TV showed higher differences in the volume averaged SEDs between hFE and μFE. The error between μFE and hFE appeared to be less affected by cortical thickness.
For the axial load case, samples with lower trabecular thickness showed larger differences. In the shear load case, samples with smaller mean trabecular separation and samples with higher mean trabecular number showed smaller differences (see Figure 3.13).

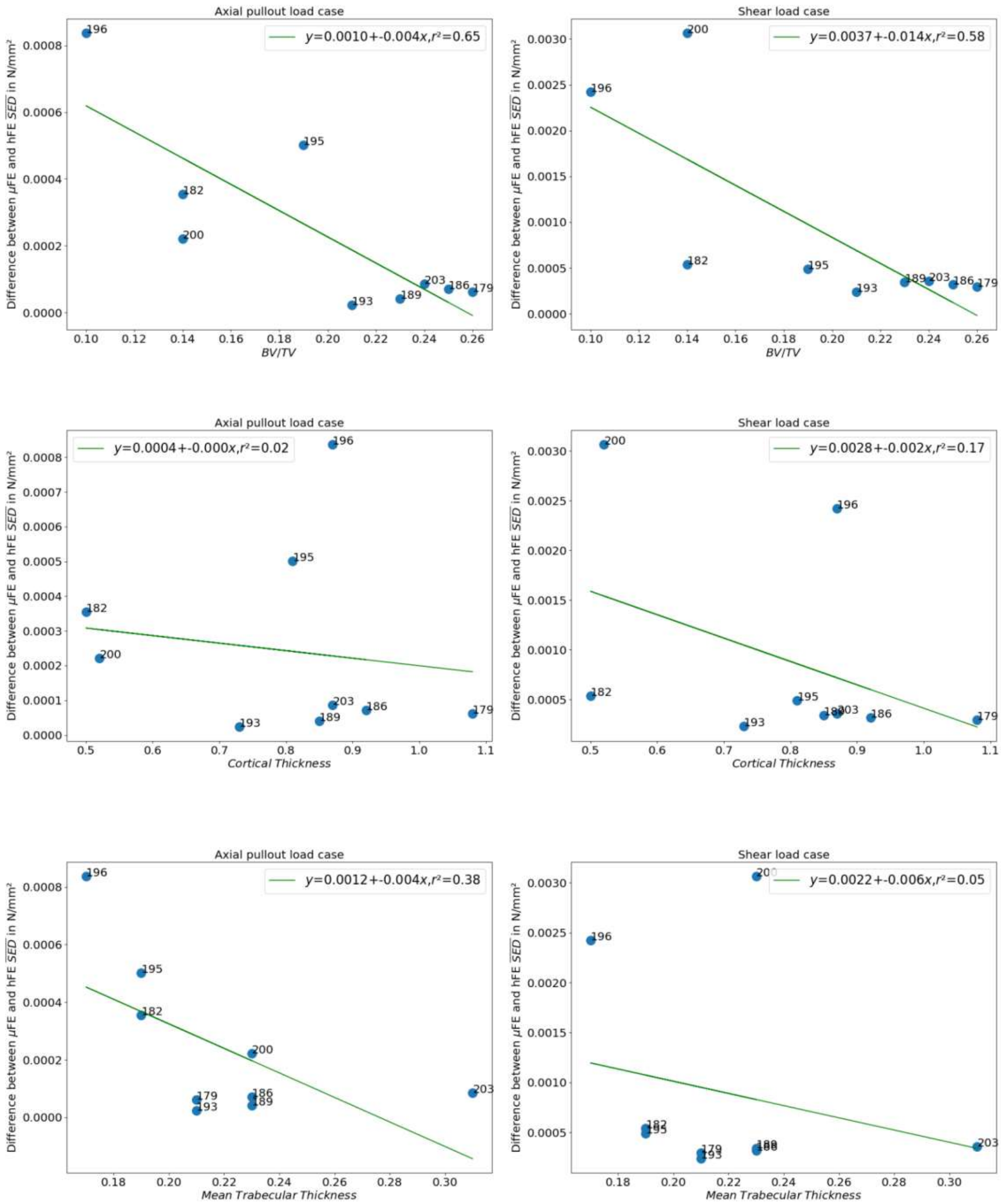

Figure 3.12: Comparison of the difference in volume averaged SED between μFE and hFE against the respective morphometric indices: trabecular BV/TV, cortical thickness and mean trabecular thickness. The left side is the axial load case and the right side is the shear load case. Specimens are annotated with the specimen ID. The statistics of the linear regression is presented in the legend: Intercept, slope and the coefficient of determination (r^2).

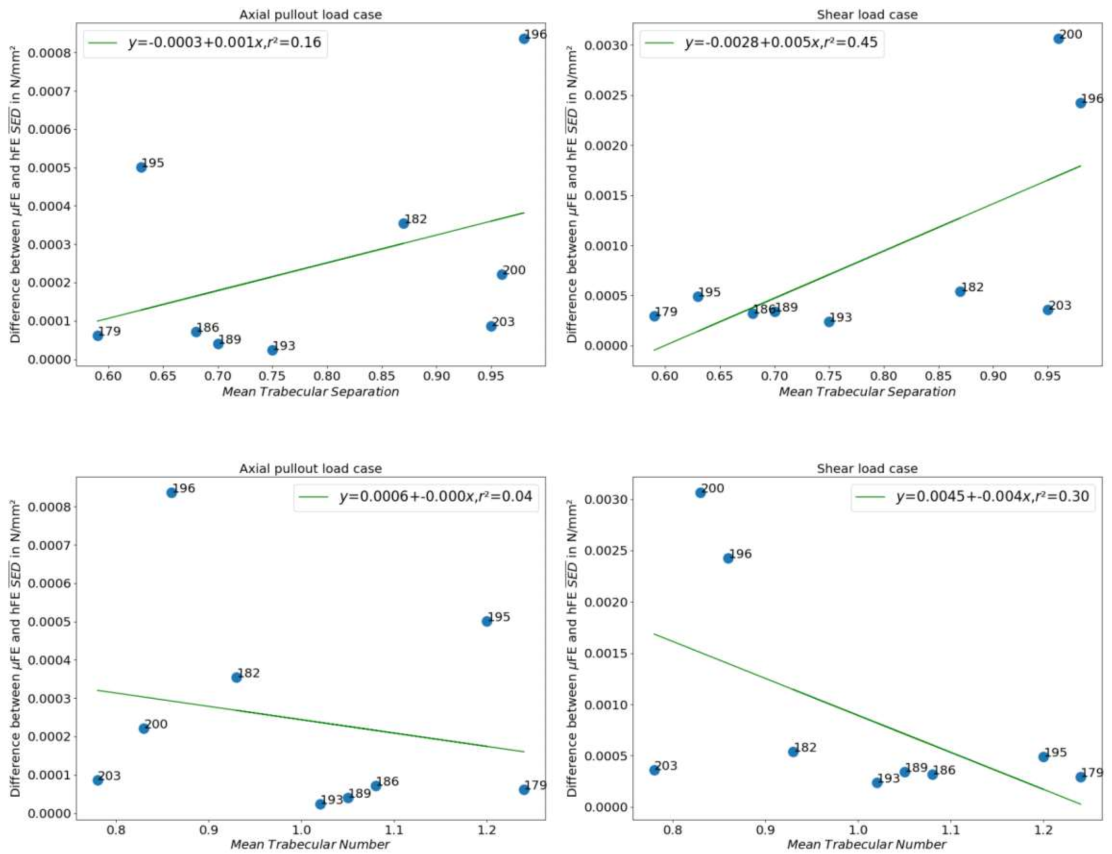

Figure 3.13: Comparison of the difference in volume averaged SED between μFE and hFE against the respective morphometric indices: mean trabecular separation and mean trabecular number. The left side is the axial load case and the right side is the shear load case. Specimens are annotated with the specimen ID.

3.5 Influence of Material Mapping

A study on the properties of trabecular bone material was performed on one exemplary specimen to compare three different modeling strategies (isotropic homogeneous, isotropic inhomogeneous and orthotropic inhomogeneous) based on stiffness and local SEDs (see section h-FE Modelling of the Methods). The trabecular BV/TV of the specimen was 0.26%.

Table 3.2 shows that in the axial pullout load case the difference in stiffness from isotropic homogeneous to orthotropic inhomogeneous was reduced by 6.55%. In the shear load case an improvement of 3.56% was achieved using inhomogeneous rather than homogeneous trabecular bone density, however, the difference from isotropic inhomogeneous to orthotropic inhomogeneous was considerably lower (0.24 %).
A linear regression analysis of the local SEDs, comparing each of the three hFE modeling strategies in both load cases to the μFE models is represented in Figure 3.14 for one exemplary specimen. The results showed that the 1:1 relation was better approximated when both the inhomogeneity of trabecular bone density and orthotropy were included. This was true for both load cases. The goodness of fit (r^2) was not improved considerably using inhomogeneous or even inhomogeneous orthotropic trabecular bone material.

Modeling strategy	Load case	Difference to the μFE stiffness (%)
Orthotropic inhomogeneous	axial pullout	20.39
Isotropic inhomogeneous	axial pullout	24.03
Isotropic homogeneous	axial pullout	26.94
Orthotropic inhomogeneous	shear	2.86
Isotropic inhomogeneous	shear	6.18
Isotropic homogeneous	shear	6.42

Table 3.2: Difference of the stiffness between hFE models to μFE models in both load cases and with different material mapping approaches.

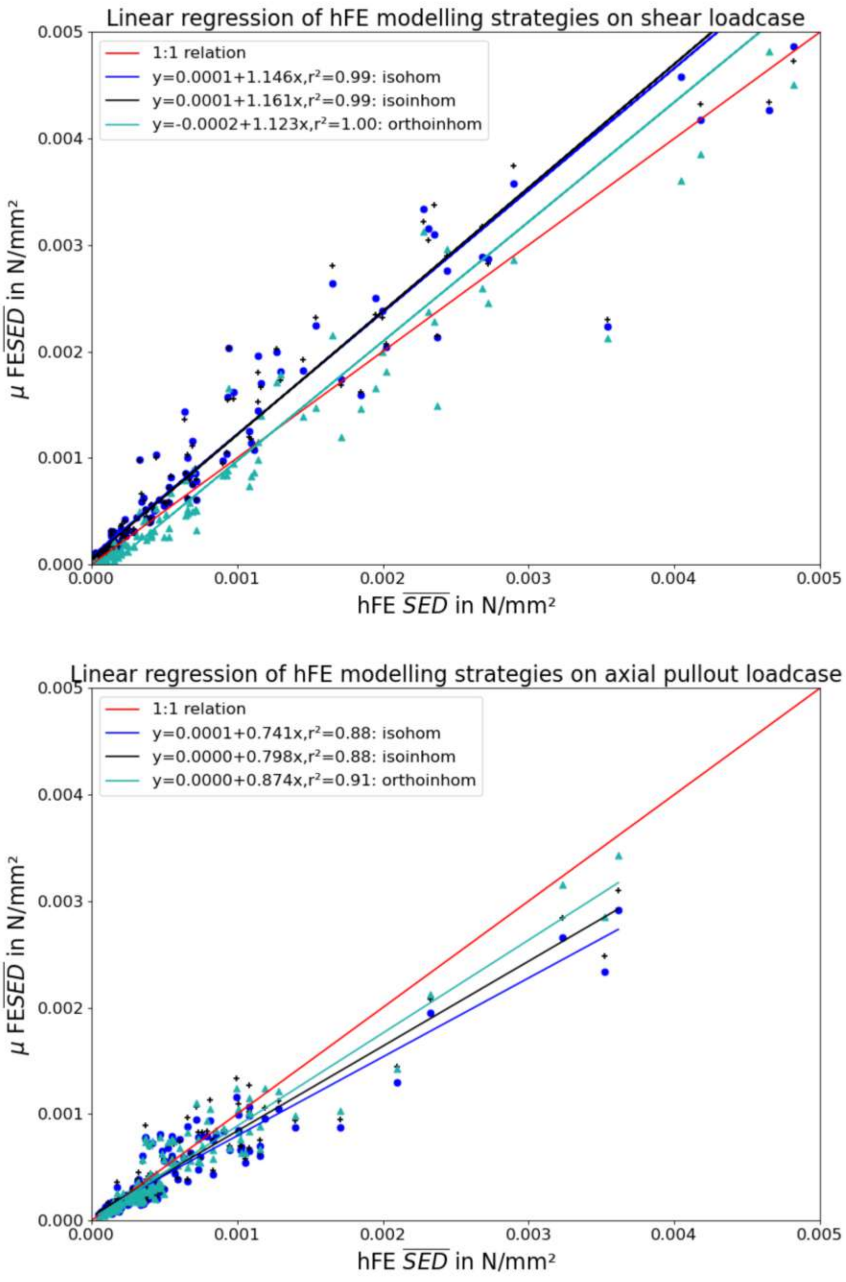

Figure 3.14: Linear regression of the local SEDs of the hFE modeling strategies for one exemplary specimen. The statistics of the linear regression are presented in the legend: Intercept, slope and the coefficient of determination (r^2). A 1:1 line is drawn in red to show an ideal relation. Isotropic homogeneous, isotropic inhomogeneous and orthotropic inhomogeneous are presented in blue, black and turquoise, respectively. Top row: shear load case; bottom row: axial pullout load case.

CHAPTER 4

Discussion

The aim of this study was to investigate the relation of hFE and μFE peri-implant volume averaged SED in bone samples including both trabecular and cortical bone in two different load cases in a single-screw bone construct. Based on nine radius sections with virtually implanted screws, it could be shown that volume averaged SEDs correlated well between hFE and μFE models in both load cases (r^2=0.96, r^2=0.84). However, a 1:1 agreement between the predictions could not be achieved. Particularly radius sections with low bone volume fraction, low trabecular thickness or large trabecular separation showed large deviations between hFE and μFE models. An in-depth discussion of these results and the limitations of this study are presented in Sections 4.1 and 4.2.

4.1 Comparison of μFE and hFE Models

The observed displacement fields between FE and hFE were qualitatively similar for both load cases (see Figure 3.1).

The mean stiffness of the hFE model in axial pullout was 8459.03±3077.91 N/mm and in shear 795.77±88.07 N/mm. The mean stiffness of the μFE model in axial pullout was 6314.23±2926.01 N/mm and in shear 659.77±100.79 N/mm. The values for axial pullout stiffness found in this study are in good agreement with the results of other studies by Chevalier et al. [40], Varga et al. [66] and Wirth et al.[67], who reported pullout stiffnesses in the range of 1700 9700 N/mm. The spring stiffness correlated well between hFE and μFE models in both load cases (r^2=0.98, r^2=0.97). However, the hFE models overestimated the stiffness in both load cases.

Possible reasons for the overestimation could be the isotropic homogeneous modeled material properties for the cortex. Another possible reason could be the material mapping law chosen since the calibration of material mapping laws could overcome stiffness errors [30, 68].

A qualitative comparison of the SED distribution showed that local peaks in the trabecular region were essentially averaged-out in the hFE models. However, the overall predicted hFE SED distributions within bone were visually consistent with the μFE results.

The volume averaged SED correlated well between the two models in the axial pullout load case (r^2=0.96, see Figure 3.7), despite the lack of a 1:1 agreement. The higher magnitudes of the volume averaged SED were apparently related to bone density (see Figure 3.2). All three VOI sizes showed a similar correlation pattern, indicating that a larger VOI did not improve the correlation, just changed the magnitude, since higher SEDs were usually in close proximity to the screw. The volume averaged SED in the μFE model was higher than in the hFE model, which was in agreement with the higher stiffness of the hFE models.

The volume averaged SED also correlated well between the two models in the shear load case (r^2=0.84, see Figure 3.8), but the slope of the regression line was close to 0.2, indicating low accuracy. All three VOI sizes showed a similar correlation as before in the axial pullout load case. Similar to the axial pullout load case, the volume averaged SED in the μFE model was higher than in the hFE model. Two specimens showed a considerably larger volume averaged SED in the μFE model compared to other specimens. The color in Figure 3.8 indicated that these two specimens had lower bone density, however, another lower bone density specimen, closer to a 1:1 agreement, did not appear to be affected by bone density alone. This led to further investigation of other morphometric indices.

The difference in volume averaged SED between μFE and hFE was compared to five different morphometric indices of trabecular and cortical bone: trabecular

BV/TV, cortical thickness, mean trabecular thickness; mean trabecular separation and mean trabecular number. This should be used to find out whether there was a dependency of the morphometric parameter and whether a threshold could be defined at which the differences did increase or decrease.

As presented in Figure 3.7 and 3.8, trabecular BV/TV was a relevant parameter for the accuracy of the volume averaged SED predicted by the hFE models. It was seen that specimens with bone density less than 20% had a larger difference in volume averaged SED (see Figure 3.12). This was demonstrated in Figure 3.10 and Figure 3.11 by comparing only specimens with a BV/TV greater than 20%. In the shear load case, the 1:1 agreement improved notably and in the axial pullout load case, a 1:1 agreement was achieved. The error between μFE and hFE appeared to be less affected by cortical thickness. For the axial load case, specimens with a smaller trabecular thickness showed larger differences. In the shear load case on the other hand, the influence of the mean trabecular separation was more pronounced (see Figure 3.13). The regression analysis of the mean trabecular number and the volume averaged SED showed that the trabecular number was not a clear indication of the difference in the case of axial loading. For the shear load case, on the other hand, a higher mean trabecular number indicated a smaller difference.

The fact that morphometry influences the predictions of stiffness and SED is in agreement with numerous studies [40, 69, 70, 71]. As a result, peri implant SEDs predicted with hFE appear accurate in high quality bone, but caution is warranted in regions of poor bone quality (e.g. low bone density, high trabecular separation, low trabecular thickness).

In order to assess the influence of the trabecular bone material modeling strategy in the hFE models on the predicted stiffness and SED distribution, three modeling strategies were compared for one specimen: isotropic homogeneous, isotropic inhomogeneous and orthotropic inhomogeneous. The results showed that the difference to the μFE models in axial pullout stiffness from isotropic homogeneous to orthotropic inhomogeneous was reduced by 6.55% and 3.56%, respectively (see Table 3.2). The results of the linear regression of the local SEDs showed that the 1:1 relation was better approximated when both the inhomogeneity of trabecular bone density and orthotropy were included. This applied to both load cases. The goodness of fit (r^2) was not improved considerably using inhomogeneous or even inhomogeneous orthotropic trabecular bone material. This finding is in agreement with Synek et al. [38], who reported that inclusion of local bone orthotropy did not improve the axial stiffness predictions of FE models of entire radii with volar locking plates.

Taken together, this study supports the approach of Varga et al. [11] to use hFE predicted peri-implant loading as a predictor of bone-implant failure. However, there appeared to be limitations in terms of bone density and other morphological parameters. Below a certain bone volume fraction, trabecular thickness, or trabecular number and above a certain trabecular separation, problems with homogenization could occur.

4.2 Limitations

This study had some limitations that should be addressed. The screws in the hFE models were modeled as cylinders without threads. The screw-bone contact interface was modelled as perfectly bonded, which is similar to the "osseointegrated" case. While this still allows a direct comparison of hFE and μFE without damage or contact as confounding factors, it must be mentioned that in reality, damage will occur, and the interface will not be tied directly after screw implantation [7, 41]. Ovesy et al. [31] and Macleod et al. [1] reported that the local stresses and strains within the bone near the screw had a significant dependence on the interface modelling. Thus, the comparison of μFE and hFE in this study are valid for secondary stability (osseointegrated), but not primary stability (directly after screw insertion).

Another limitation was that isotropic homogeneous bone material properties were used for the cortical shell. The inclusion of porosity in the cortex of the hFE model might further improve the results [19, 72]. Further parametric studies should be performed to find limitations in the accuracy of hFE models with the inclusion of porosity in the cortex.

Finally, only nine specimens and one screw model were used. The screw insertion depth and position were the same for each sample and the same two load cases were applied. Further studies with additional specimens, additional anatomical locations and screw-in depth positions should be considered.

4.3 Conclusions

In a clinical scenario (i.e., including both trabecular bone and cortex) of a single screw-bone construct located at the distal radius, a significant correlation was found between the peri-implant volume average strain energy densities (SED) and the spring stiffness of hFE and μFE models in two load cases. hFE models generally overestimated the stiffness and underestimated the volume average SEDs. Cortical bone material properties or the material law calibration could have caused this discrepancy. The difference between hFE and μFE also showed a dependence on bone morphometric parameters and was particularly high for samples with low bone volume fraction. A sub-study on the trabecular bone material modelling strategy in the hFE models showed that local bone orthotropy only marginally improved the accuracy and precision of the prediction of the SED distribution.
Overall, this study showed that hFE models are able to predict volume averaged peri implant SEDs of screw bone constructs in good agreement with μFE results, but this agreement may deteriorate drastically for bone samples with low bone volume quality.

List of Figures

List of Tables

List of Algorithms

Bibliography

[1] Alisdair R. MacLeod, Pankaj Pankaj, and A. Hamish R.W. Simpson. Does screw bone interface modelling matter in finite element analyses? *Journal of Biomechanics*, 45, 2012.

[2] Thomas A. Decoster, David B. Heetderks, Daniel J. Downey, James S. Ferries, and Wendell Jones. Optimizing bone screw pullout force, 1990.

[3] Kristophe Karami, Laura Buckenmeyer, Ata Kiapour, Prashant Kelkar, Constantine Demetropoulos, and Teck Soo. Biomechanical evaluation of the pedicle screw insertion depth effect on screw stability under cyclic loading and subsequent pullout. *Journal of spinal disorders techniques*, 28, 10 2014.

[4] Herwig Drobetz, Patrick Weninger, Caroline Grant, Clare Heal, Reinhold Muller, Michael Schuetz, Minh Pham, and Roland Steck. More is not necessarily better. a biomechanical study on distal screw numbers in volar locking distal radius plates. *Injury*, 44:535 539, 2013.

[5] Isabella Mehling, Lars P. Müller, Katharina Delinsky, Dorothea Mehler, Dipl Ing, Klaus J. Burkhart, and Pol M. Rommens. Number and Locations of Screw Fixation for Volar Fixed-Angle Plating of Distal Radius Fractures: Biomechanical Study. *Journal of Hand Surgery*, 35(6):885 891, 2010.

[6] Junichi Miyake, Tsuyoshi Murase, Hisao Moritomo, Kazuomi Sugamoto, and Hideki Yoshikawa. Distal radius osteotomy with volar locking plates based on computer simulation. *Clinical Orthopaedics and Related Research®*, 469:1766 1773, 2011.

[7] Juri A. Steiner, Patrik Christen, Remo Affentranger, Stephen J. Ferguson, and Gerrit Harry van Lenthe. A novel in silico method to quantify primary stability of screws in trabecular bone. *Journal of Orthopaedic Research*, 35(11):2415 2424, nov 2017.

[8] Franz Kralinger, Michael Blauth, Jörg Goldhahn, Kurt Kach, Christine Voigt, Andreas Platz, and Beate Hanson. The influence of local bone density on the outcome of one hundred and fifty proximal humeral fractures treated with a locking plate. *Journal of Bone and Joint Surgery - American Volume*, 96(12):1026 1032, 2014.

[9] Vasiliki C. Panagiotopoulou, Marzieh Ovesy, Boyko Gueorguiev, R. Geoff Richards, Philippe Zysset, and Peter Varga. Experimental and numerical investigation of secondary screw perforation in the human proximal humerus. *Journal of the Mechanical Behavior of Biomedical Materials*, 116:104344, 2021.

[10] Jan Christoph Katthagen, Michael Schwarze, Mara Warnhoff, Christine Voigt, Christof Hurschler, and Helmut Lill. Influence of plate material and screw design on stiffness and ultimate load of locked plating in osteoporotic proximal humeral fractures. *Injury*, 47(3):617 624, 2016.

[11] Peter Varga, Leonard Grünwald, Jason A. Inzana, and Markus Windolf. Fatigue failure of plated osteoporotic proximal humerus fractures is predicted by the strain around the proximal screws. *Journal of the Mechanical Behavior of Biomedical Materials*, 75:68 74, nov 2017.

[12] Samuel N. Crosby, Nicholas D. Fletcher, Erwin R. Yap, and Donald H. Lee. The mechanical stability of extra-articular distal radius fractures with respect to the number of screws securing the distal fragment. *The Journal of Hand Surgery: British European Volume*, 38:1097 1105, 2013.

[13] Jason A. Inzana, Peter Varga, and Markus Windolf. Implicit modeling of screw threads for efficient finite element analysis of complex bone-implant systems. *Journal of Biomechanics*, 2016.

[14] Dieter H. Pahr and Philippe K. Zysset. A comparison of enhanced continuum fe with micro fe models of human vertebral bodies. *Journal of Biomechanics*, 42(4):455 462, 2009.

[15] Peter Varga, Enrico Dall'Ara, Dieter H. Pahr, Michael Pretterklieber, and Philippe K. Zysset. Validation of an hr-pqct-based homogenized finite element approach using mechanical testing of ultra-distal radius sections. *Biomechanics and Modeling in Mechanobiology*, 10:431 444, 2011.

[16] Jan Wolff, Nathaniel Narra, Anna-Kaisa Antalainen, Jiří Valášek, Jozef Kaiser, George K. Sándor, and Petr Marcián. Finite element analysis of bone loss around failing implants. *Materials Design*, 61:177 184, 2014.

[17] Amnon Sharir, Meir Max Barak, and Ron Shahar. Whole bone mechanics and mechanical testing. *The Veterinary Journal*, 177:8 17, 2008.

[18] Matthew J. Olszta, Xingguo Cheng, Sang Soo Jee, Rajendra Kumar, Yi-Yeoun Kim, Michael J. Kaufman, Elliot P. Douglas, and Laurie B. Gower. Bone structure and formation: A new perspective. *Materials Science and Engineering: R: Reports*, 58:77 116, 2007.

[19] Jae-Young Rho, Liisa Kuhn-Spearing, and Peter Zioupos. Reprinted from elsevier science with permission from elsevier mechanical properties and the hierarchical structure of bone. *Medical Engineering Physics*, 20:92 102, 1998.

[20] Elise F. Morgan, Ginu U. Unnikrisnan, and Amira I. Hussein. Bone mechanical properties in healthy and diseased states. *Annual Review of Biomedical Engineering*, 20:119 143, 2018.

[21] Richard B. Ashman and Jae Young Rho. Elastic modulus of trabecular bone material. *Journal of Biomechanics*, 21:0 181, 1988.

[22] Tony M. Keaveny, Elise F. Morgan, Glen L. Niebur, and Oscar C. Yeh. Biomechanics of trabecular bone. *Annual Review of Biomedical Engineering*, 3:307 333, 2001.

[23] A. Gefen. Optimizing the biomechanical compatibility of orthopedic screws for bone fracture fixation. *Medical Engineering Physics*, 24:337 347, 2002.

[24] E.A. Friis, T.A. DeCoster, and J.C. Thomas. Mechanical testing of fracture fixation devices. In Elizabeth Friis, editor, *Mechanical Testing of Orthopaedic Implants*, pages 131 141. Woodhead Publishing, 2017.

[25] Joern Seebeck, Joerg Goldhahn, Michael M. Morlock, and Erich Schneider. Mechanical behavior of screws in normal and osteoporotic bone. *Osteoporosis International*, 16:S107 S111, 2005.

[26] Yuehuei H An. *Internal fixation in osteoporotic bone*. Thieme, 1 edition, 2002.

[27] B. W. Bufkin, M. D. Barnhart, A. J. Kazanovicz, S. J. Naber, and S. C. Kennedy. The effect of screw angulation and insertion torque on the push-out strength of polyaxial locking screws and the single cycle to failure in bending of polyaxial locking plates. *Veterinary and Comparative Orthopaedics and Traumatology*, 26:186 191, 2013.

[28] Petr Marcián, Libor Borák, Tomáš Zikmund, Ladislava Horáčková, Jozef Kaiser, Marek Joukal, and Jan Wolff. On the limits of finite element models created from (micro)ct datasets and used in studies of bone-implant-related biomechanical problems. *Journal of the Mechanical Behavior of Biomedical Materials*, 117:104393, 2021.

[29] Francesco Pappalardo, Giulia Russo, Flora Musuamba Tshinanu, and Marco Viceconti. In silico clinical trials: concepts and early adoptions. *Briefings in Bioinformatics*, 2018.

[30] Dieter H. Pahr and Philippe K. Zysset. Finite element-based mechanical assessment of bone quality on the basis of in vivo images. *Current Osteoporosis Reports*, 14:374 385, 2016.

[31] Marzieh Ovesy, Benjamin Voumard, and Philippe Zysset. A nonlinear homogenized finite element analysis of the primary stability of the bone implant interface. *Biomechanics and Modeling in Mechanobiology*, 17(5):1471 1480, oct 2018.

[32] Saba Saeb, Paul Steinmann, and Ali Javili. Aspects of computational homogenization at finite deformations: A unifying review from reuss' to voigt's bound. *Applied Mechanics Reviews*, 68:050801, 2016.

[33] Dieter H. Pahr and Philippe K. Zysset. Influence of boundary conditions on computed apparent elastic properties of cancellous bone. *Biomechanics and Modeling in Mechanobiology*, 7:463 476, 2008.

[34] Martin Ostoja-Starzewski. Material spatial randomness: From statistical to representative volume element. *Probabilistic Engineering Mechanics*, 21:112 132, 2006.

[35] Sander Poelert, Edward Valstar, Harrie Weinans, and Amir A. Zadpoor. Patient-specific finite element modeling of bones. *Proceedings of the Institution of Mechanical Engineers Part H Journal of Engineering in Medicine*, 227:464 478, 2013.

[36] Fulvia Taddei, Alberto Pancanti, and Marco Viceconti. An improved method for the automatic mapping of computed tomography numbers onto finite element models. *Medical Engineering Physics*, 26(1):61 69, 2004.

[37] Philippe K. Zysset and Alain Curnier. An alternative model for anisotropic elasticity based on fabric tensors. *Mechanics of Materials*, 21:243 250, 1995.

[38] Alexander Synek, Yan Chevalier, and Dieter H. Baumbach, Sebastian F.; Pahr. The influence of bone density and anisotropy in finite element models of distal radius fracture osteosynthesis: Evaluations and comparison to experiments. *Journal of Biomechanics*, page S0021929015005606, 2015.

[39] Andreas J. Wirth, Ralph Müller, and G. Harry van Lenthe. The discrete nature of trabecular bone microarchitecture affects implant stability. *Journal of Biomechanics*, 45(6):1060 1067, 2012.

[40] Yan Chevalier. Numerical Methodology to Evaluate the Effects of Bone Density and Cement Augmentation on Fixation Stiffness of Bone-Anchoring Devices. *Journal of Biomechanical Engineering*, 137(9):1 10, 2015.

[41] Juri A. Steiner, Stephen J. Ferguson, and G. Harry van Lenthe. Computational analysis of primary implant stability in trabecular bone. *Journal of Biomechanics*, 48:807 815, 2015.

[42] Jan Wieding, Robert Souffrant, Andreas Fritsche, Wolfram Mittelmeier, Rainer Bader, and Boris Rubinsky. Finite element analysis of osteosynthesis screw fixation in the bone stock: An appropriate method for automatic screw modelling. *PLoS ONE*, 7:e33776, 2012.

[43] Emmanuel Tetteh and Matthew B. A. McCullough. Impact of screw thread shape on stress transfer in bone: a finite element study. *Computer Methods in Biomechanics Biomedical Engineering*, pages 1 6, 2020.

[44] Marzieh Ovesy, Michael Indermaur, and Philippe Zysset. Prediction of insertion torque and stiffness of a dental implant in bovine trabecular bone using explicit micro-finite element analysis. *Journal of the Mechanical Behavior of Biomedical Materials*, 98, 07 2019.

[45] Hadi S. Hosseini, Andreas Dünki, Jonas Fabech, Martin Stauber, Nicolas Vilayphiou, Dieter Pahr, Michael Pretterklieber, Jasmin Wandel, Bert van Rietbergen, and Philippe K. Zysset. Fast estimation of colles' fracture load of the distal section of the radius by homogenized finite element analysis based on hr-pqct. *Bone*, 97:65 75, 2017.

[46] Andrés J. Arias-Moreno, Hadi S. Hosseini, Melissa Bevers, Keita Ito, Philippe K. Zysset, and Bert van Rietbergen. Validation of distal radius failure load predictions by homogenized- and micro-finite element analyses based on second-generation high-resolution peripheral quantitative ct images. *Osteoporosis International*, 2019.

[47] Denis Schenk, Andrea Mathis, Kurt Lippuner, and Philippe Zysset. In vivo repeatability of homogenized finite element analysis based on multiple hr-pqct sections for assessment of distal radius and tibia strength. *Bone*, page 115575, 2020.

[48] Monika Stipsitz, Philippe K. Zysset, and Dieter H. Pahr. Prediction of the Inelastic Behaviour of Radius Segments: Damage-based Nonlinear Micro Finite Element Simulation vs Pistoia Criterion. *Journal of Biomechanics*, 116:110205, feb 2021.

[49] Michael Smith. *ABAQUS/Standard User's Manual, Version 6.9*. Dassault Systèmes Simulia Corp, United States, 2009.

[50] Cyril Flaig. *A highly scalable memory efficient multigrid solver for μ-finite element analyses*. PhD thesis, ETH Zurich, Zürich, 2012.

[51] Guido Van Rossum and Fred L. Drake. *Python 3 Reference Manual*. CreateSpace, Scotts Valley, CA, 2009.

[52] Ron Kikinis, Steve Pieper, and Kirby Vosburgh. *3D Slicer: A Platform for Subject-Specific Image Analysis, Visualization, and Clinical Support*, volume 3, pages 277 289. 01 2014.

[53] Yasukazu Totoki, Yuichi Yoshii, Takuya Kusakabe, Kenichi Akita, and Tomoo Ishii. Screw length optimization of a volar locking plate using three dimensional preoperative planning in distal radius fractures. *The Journal of Hand Surgery (Asian-Pacific Volume)*, 23:520 527, 2018.

[54] Mary L Bouxsein, Stephen K Boyd, Blaine A Christiansen, Robert E Guldberg, Karl J Jepsen, and Ralph Müller. Guidelines for assessment of bone microstructure in rodents using micro computed tomography. *Journal of Bone and Mineral Research*, 25:1468 1486, 2010.

[55] Monika Stipsitz. *Development of a nonlinear micro finite element framework for image-based simulations in bone biomechanics*. PhD thesis, Wien, 2020.

[56] Thomas Gross, Dieter Pahr, and Philippe Zysset. Morphology-elasticity relationships using decreasing fabric information of human trabecular bone from three major anatomical locations. *Biomechanics and modeling in mechanobiology*, 12, 10 2012.

[57] The CGAL Project. *CGAL User and Reference Manual*. CGAL Editorial Board, 5.4 edition, 2022.

[58] Steve A. Maas, Benjamin J. Ellis, David S. Rawlins, and Jeffrey A. Weiss. Finite element simulation of articular contact mechanics with quadratic tetrahedral elements. *Journal of Biomechanics*, 2016.

[59] G. L. Niebur, J. C. Yuen, A. C. Hsia, and T. M. Keaveny. Convergence behavior of high-resolution finite element models of trabecular bone. *Journal of Biomechanical Engineering*, 121:629, 1999.

[60] Thomas Gross, Dieter H. Pahr, and Philippe K. Zysset. Morphology elasticity relationships using decreasing fabric information of human trabecular bone from three major anatomical locations. *Biomechanics and Modeling in Mechanobiology vol. 12 iss. 4*, 12, oct 2012.

[61] Philippe K. Zysset. A review of morphology elasticity relationships in human trabecular bone: theories and experiments. *Journal of Biomechanics*, 36:1469 1485, 2003.

[62] David Freedman. *Statistical Models : Theory and Practice*. Cambridge University Press, August 2005.

[63] J. Martin Bland and Douglas G. Altman. Statistical methods for assessing agreement between two methods of clinical measurement. *International Journal of Nursing Studies*, 47:931 936, 2010.

[64] Alexander Synek, Sebastian Baumbach, and Dieter Pahr. Towards optimization of volar plate fixations of distal radius fractures: Using finite element analyses to reduce the number of screws. *Clinical Biomechanics*, 82:105272, 01 2021.

[65] Cornelius O. Horgan. On the strain-energy density in linear elasticity. *Journal of Engineering Mathematics*, 7:231 234, 1973.

[66] Peter Varga, Sebastian Baumbach, Dieter Pahr, and Philippe K. Zysset. Validation of an anatomy specific finite element model of colles' fracture. *Journal of Biomechanics*, 42:1726 1731, 2009.

[67] Andreas J. Wirth, Ralph Müller, and G. Harry van Lenthe. Augmentation of peri-implant bone improves implant stability: Quantification using simulated bone loss. *Journal of Orthopaedic Research*, 30:178 184, 2012.

[68] E. Verhulp, B. van Rietbergen, and R. Huiskes. Comparison of micro-level and continuum-level voxel models of the proximal femur. *Journal of Biomechanics*, 39:2951 2957, 2006.

[69] C. M. Hughes, A. Bordush, B. Robioneck, P. Procter, and C. J. Brown. Bone anchors-a preliminary finite element study of some factors affecting pullout. *Journal of Medical Devices, Transactions of the ASME*, 8(4):1 9, 2014.

[70] Adeliya Latypova, Ghislain Maquer, Kaliyaperumal Elankumaran, Dieter Pahr, Philippe Zysset, Dominique P. Pioletti, and Alexandre Terrier. Identification of elastic properties of human patellae using micro finite element analysis. *Journal of Biomechanics*, 2016.

[71] Tsutomu Sugiura, Kazuhiko Yamamoto, Satoshi Horita, Kazuhiro Murakami, Sadami Tsutsumi, and Tadaaki Kirita. The effects of bone density and crestal cortical bone thickness on micromotion and peri-implant bone strain distribution in an immediately loaded implant: a nonlinear finite element analysis. *Journal of Periodontal Implant Science*, 46:152, 2016.

[72] X Neil Dong and X Edward Guo. The dependence of transversely isotropic elasticity of human femoral cortical bone on porosity. *Journal of Biomechanics*, 37:1281 1287, 2004.